Title
On the Physical Accuracy of Scalar Transport Modeling in Inhomogeneous Turbulence

Authors
Bernard, P.S.
Rovelstad, A.L.

Publication Date
1993-08-01

LBL-33535
UC-405
Preprint

Lawrence Berkeley Laboratory
UNIVERSITY OF CALIFORNIA

Physics Division

Mathematics Department

Submitted for publication

On the Physical Accuracy of Scalar Transport Modeling in Inhomogeneous Turbulence

P.S. Bernard and A.L. Rovelstad

August 1993

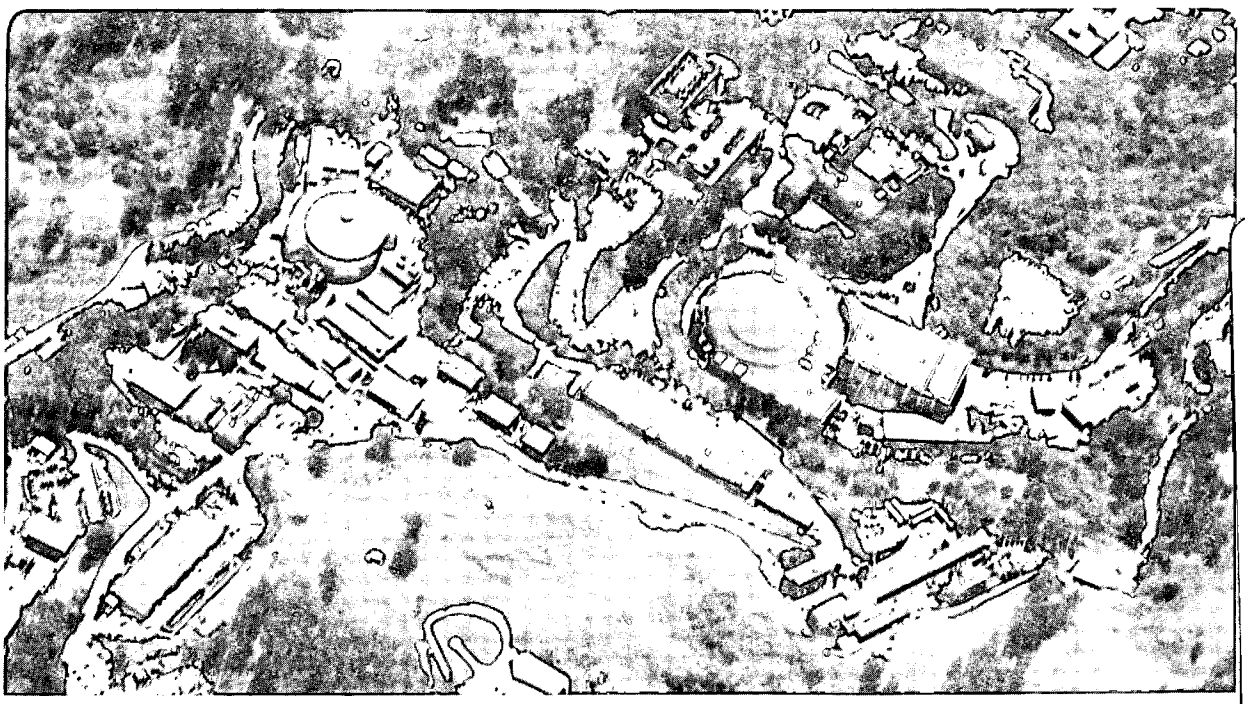

Prepared for the U.S. Department of Energy under Contract Number DE-AC03-76SF00098

DISCLAIMER

DISCLAIMER

LBL-33535

ON THE PHYSICAL ACCURACY OF SCALAR TRANSPORT MODELING IN INHOMOGENEOUS TURBULENCE[1]

Peter S. Bernard[2]
Department of Mathematics
and
Lawrence Berkeley Laboratory
University of California
Berkeley, CA 94720

and

Amy L. Rovelstad
NRC Postdoctoral Fellow
Naval Research Laboratory
Washington, D.C. 20375

August, 1993

[1]This work was supported in part by the Office of Basic Energy Sciences, U. S. Department of Energy grant DE-FG05-88ER13838 and in part by the Applied Mathematical Sciences Subprogram of the Office of Energy Research, U. S. Department of Energy under Contract DE-AC03-76SF00098. Computer time was supplied in part by the Pittsburgh Supercomputing Center.

[2]Permanent address: Department of Mechanical Engineering, University of Maryland, College Park, MD 20742

ABSTRACT

Direct numerical simulations of scalar fields produced by uniform and line sources in channel flow are used as the basis for examining the accuracy of random flight and closure models in predicting turbulent scalar transport rates. Closure models of gradient form with an anisotropic eddy diffusivity tensor perform well for the uniform source flow and the far field of plumes. In the near field, the plume is seriously distorted due to the inappropriateness of gradient transport in modeling the streamwise flux rate. Random flight models are most successful in producing a qualitative rendering of the near field of the plume, but are subject to significant quantitative inaccuracies. Ensembles of particle paths having common endpoints are used to explore the physics of the transport correlation. For plume flows, transport in the near field is primarily due to the average effect of the meandering of the turbulent fluid over the source, in which the scalar gained by fluid particles correlates with the local velocity fluctuations. Further downstream, displacement transport – which may be reasonably modeled via gradient physics – emerges as the principal mechanism behind the scalar flux.

I. INTRODUCTION

Thermal and mass concentration fields diffusing within turbulent shear flows are found in many guises in environmental science and engineering. Current methods for numerically predicting such phenomena are largely confined to solutions of the Reynolds averaged equations for which the turbulent scalar flux rate must be modeled[1–3] and random flight models which mimic the motion of individual tracers in turbulence through an assumed Markov process[4–6]. Since the physical processes underlying the turbulent flux of scalar contaminants are only partially understood at the present time, closure models for the scalar transport correlation have tended to adopt the gradient form. Numerous examples of non-gradient transport are known to exist in applications[7], however, and it has long been recognized[7–9] that gradient transport is incapable of representing the short time dispersion near the source of contaminant plumes under even homogeneous conditions. The limitations of gradient models and the success of random flight models in capturing short time diffusion in homogeneous turbulence, have been an impetus for the extension and application of random flight models to inhomogeneous flows. Since gradient transport models are compatible with plume growth in the far field, however, they have remained a desirable choice in such situations.

Random flight algorithms suitable for non-homogeneous turbulence have seen widespread use in meteorological[4–6,10–12] and engineering[13] applications. Though the 'well-mixed' criterion[14] provides necessary conditions on all moments of the random velocity increments of the tracers, practical considerations require that random flight models be applied under simplifying assumptions. Many tests of the predictions of such models have been made against experimental data, sometimes including direct comparisons between random flight and closure models. On the whole, however, such studies have not been in controlled settings where accurate information about the turbulence scales and other correlations appearing in the models are available. As a result, it has been difficult to discern what the relative strengths of the two methodologies are, and especially if the substantially greater computational cost of random flight methods in comparison to closure models pays off in the form of greater accuracy in the prediction of the near field of scalar dispersal.

Direct numerical simulations (DNS) of turbulent flows including scalar transport, provide a useful setting from which to carry out objective tests of prediction techniques[2,3,15]. In particular, all of the necessary fluid mechanical correlations – including time and length scales – needed in implementing scalar diffusion algorithms can be computed from the simulated flow. Scalar transport fluxes and the mean scalar field itself can also be known to

any desired extent, so the predictions of the various theories can be tested without ambiguity. The wealth of information provided by DNS has also spawned a number of studies[16–20] seeking to establish relationships between scalar transport and the underlying turbulent fluid motion. Such knowledge may be instrumental in deriving future improvements to prediction techniques.

The interest of the current work is twofold. First we use a DNS of diffusing scalar fields in a turbulent channel flow to assess the performance and physical integrity of scalar transport models under conditions where the turbulence is inhomogeneous. Secondly, we examine the relationship between current gradient type closure models and the actual physical mechanisms leading to the scalar flux correlation. The intent is to develop an understanding of the physics of transport in the near field of plumes to aid in deriving physically accurate closure models. We consider scalar fields in a turbulent channel flow created by uniform and line sources. In the case of the former, zero boundary conditions are applied so that the fully developed scalar field is one-dimensional, i.e., losses of scalar through the boundary by diffusion balance its internal production. This flow has been considered in several previous studies[2,15–17]. The second example of interest consists of plumes developing downstream of spanwise-oriented line sources with zero flux, i.e., insulated, wall boundary conditions. In one case the source is held at $y^+ = 15$ and the other it is at $y^+ = 30$. The developing plumes are two-dimensional in the mean and are strongly affected by the shear and anisotropy of the channel flow.

Our exploration of the physics of scalar transport is through application of a formal analysis of ensembles of fluid particle paths computed from a direct numerical simulation of turbulent channel flow. The approach has been applied extensively in previous work to study the rates of momentum[21] and vorticity[22–23] transport. Subsequently, this was extended[24] to include the effects of vortical structures in causing Reynolds stress. The methodology finds immediate application in explaining the physical nature of scalar transport. The present study initiates such an investigation in the context of the DNS of the uniform and line source scalar fields. For the plume flow, the nature of transport near the source is considered, including how the physical transport mechanisms change with downstream distance. The degree to which gradient diffusion plays a legitimate role in the transport physics is explained, as are the physical processes which should be taken into account in a physically appropriate model.

The next section considers some of the current trends in modeling scalar fluxes and their relationship to the physics of transport as viewed through the Lagrangian technique. We

then consider in turn the uniform and line source flows in which we directly compare the predictions of closure and random flight models. In the last two sections we provide an analysis of the physics of the transport correlation in plumes and then present conclusions.

II. TRANSPORT MODELS

We consider the diffusion of a passive scalar, C, satisfying the convective diffusion equation

$$\frac{\partial C}{\partial t} + U_i \frac{\partial C}{\partial x_i} = \frac{1}{ReSc} \frac{\partial^2 C}{\partial x_i^2} + Q \tag{1}$$

where U_i is the turbulent velocity field, Q is a non-random source term, Sc is the Schmidt number and Re the Reynolds number. Alternatively, in the case of the passive diffusion of internal energy, C may be considered to be the temperature in which case Sc is replaced by the Prandtl number, Pr. After averaging, (1) yields

$$\frac{\partial \overline{C}}{\partial t} + \overline{U}_i \frac{\partial \overline{C}}{\partial x_i} = \frac{1}{ReSc} \frac{\partial^2 \overline{C}}{\partial x_i^2} - \frac{\partial \overline{u_i c}}{\partial x_i} + Q \tag{2}$$

where $\overline{C}$ and $\overline{U}_i$ are ensemble averaged means, c and u_i are fluctuations, $C = \overline{C} + c$ and $U_i = \overline{U}_i + u_i$. Closure to (2) depends on modeling the scalar flux rate, $\overline{u_i c}$. Most commonly this is done via a gradient law of the form

$$\overline{u_i c} = -K_{ij} \frac{\partial \overline{C}}{\partial x_j} \tag{3}$$

where K_{ij} is an anisotropic eddy diffusivity tensor. Our intent here is to develop a formal treatment of $\overline{u_i c}$ so that (3) can be viewed from a perspective in which the proper form for K_{ij} is revealed as well as the relative magnitude that (3) occupies among all of the physical processes causing transport.

Analysis of $\overline{u_i c}$ proceeds by a Lagrangian technique[21-23] generalizing a methodology developed by Taylor[8]. At a given point a in the flow, the transport correlation $\overline{u_i c}$ is expanded via the identity

$$\overline{u_{i_a} c_a} = \overline{u_{i_a} c_b} + \overline{u_{i_a}(\overline{C}_b - \overline{C}_a)} + \overline{u_{i_a}(C_a - C_b)} \tag{4}$$

where the subscript b denotes quantities evaluated at the random locations at time $-\tau$ of a large ensemble of fluid particles selected by their common property of arriving at point a after traveling over the time interval τ. As discussed in related contexts and verified numerically[21-23], the mixing condition $\overline{u_{i_a} c_b} = 0$ is satisfied for τ large enough. We define

the mixing time, say τ_m, as the smallest interval at which $\overline{u_{i_a} c_b} \approx 0$. τ_m may be thought of as the time over which events in the flow cause the correlation between u_i and c to develop. Equation (4) thus shows that for times $\tau > \tau_m$, $\overline{u_i c}$ is a result of the processes represented by the last two terms in (4).

The second term on the right-hand side of (4) represents transport arising from the displacement of fluid particles. It is a formal statement of the classical argument to the effect that in the presence of a gradient in the mean scalar field, turbulent eddying motion should lead to a net transport. In particular, the resulting directional dependence of the scalar flux on the gradient of $\overline{C}$ is created by fluid particles carrying on average – without alteration – the local mean scalar field of their starting point to their final point over a mixing time.

Non-gradient sources of transport are contained in the last term in (4) which can be expanded as

$$\overline{u_{i_a}(C_a - C_b)} = \frac{1}{ReSc} \int_{-\tau}^{0} \overline{u_{i_a} \nabla^2 C(s)} ds + \int_{-\tau}^{0} \overline{u_{i_a} Q(s)} ds \tag{5}$$

after integrating (1) along a particle path from b to a and substituting for $C_a - C_b$. Here, $\nabla^2 C(s)$ and $Q(s)$ denote evaluation of $\nabla^2 C$ and Q, respectively, at the position of a fluid particle at time s. The first term on the right-hand side represents the correlation between u_i and the cumulative changes to the scalar field of a fluid particle by molecular diffusion along its path. The second term in (5) expresses the transport resulting from fluid particles acquiring the scalar as they pass through the source. Each of these terms will later be shown to play an important role in the plume flow.

The displacement term in (4) can be expanded using a Taylor series representation of $\overline{C}_b$ yielding

$$\overline{u_{i_a}(\overline{C}_b - \overline{C}_a)} = -\int_{-\tau}^{0} \overline{u_i(0) u_j(s)} ds \frac{\partial \overline{C}}{\partial x_j} + \Phi_1 \tag{6}$$

where Φ_1 contains expressions originating in the higher order terms in the $\overline{C}_b$ expansion. In a steady, linearly varying, scalar mean field this term is identically zero. It is clear from (6) that the eddy diffusivity in (3) will be compatible with the underlying physics of the transport correlation if

$$K_{ij} = \int_{-\tau}^{0} \overline{u_i(0) u_j(s)} ds. \tag{7}$$

When τ is large enough so that $\overline{u_i(0) u_j(s)} = 0$ for $\mid s \mid > \tau$, (7) can be expressed more simply as

$$K_{\alpha\beta} = T_{\alpha\beta} \overline{u_\alpha u_\beta}, \tag{8}$$

where Greek indices are not summed and we have introduced a Lagrangian integral time scale through

$$\overline{u_\alpha u_\beta}\, T_{\alpha\beta} \equiv \int_{-\infty}^{0} \overline{u_\alpha(0) u_\beta(s)}\, ds. \tag{9}$$

In summary, if $\overline{u_i c}$ were entirely due to gradient transport, so that (3) were exactly true, then K_{ij} would have to be given by (8). As it stands, however, if Φ_1 in (6) and the terms given in (5) are not zero, as they very likely will not be under most circumstances, then by assuming (3) is true, one is in effect using K_{ij} to account for both gradient and non-gradient physical processes. In this case it cannot be expected that (8) will hold.

Anisotropy of K_{ij} is essential for a reasonable treatment of the wall bounded flows considered here. For example, in the case of a unidirectional flow where $\overline{C} = \overline{C}(y)$ and diffusion is in the wall-normal direction y, it is well recognized[25] that the model

$$\overline{vc} = -\nu_c \frac{d\overline{C}}{dy}, \tag{10}$$

where ν_c is the scalar eddy diffusivity, must have

$$\nu_c = T\overline{v^2} \tag{11}$$

where T is an appropriate time scale, often set equal to $2k/\epsilon$. Recently developed high Reynolds number models for scalar transport[1,26] which take

$$\nu_c \propto \frac{k^3}{\epsilon^2} \frac{d\overline{U}}{dy} \tag{12}$$

cannot be meaningfully applied near boundaries since in effect they replace $\overline{v^2}$ by k which have wholly different behaviors. Consequently, we limit the models under consideration to those which are consistent with (11) as a minimum condition.

It is common practice in turbulence modeling to introduce a turbulent Schmidt number σ_c so that ν_c can be written as $\nu_c = \nu_t/\sigma_c$ where ν_t is the eddy viscosity appearing in the Reynolds stress model

$$\overline{uv} = -\nu_t \frac{d\overline{U}}{dy}. \tag{13}$$

However, a formal analysis of momentum transport along the same lines leading to (6) shows that the theoretically correct eddy viscosity for momentum transport[21] is identical to (8). This suggests, in agreement with other analyses[27], that one should have $\nu_t = \nu_c$, i.e., that the physical mechanism underlying gradient transport does not distinguish between scalar and momentum transport. The fact that it is often necessary to assume that $\nu_t \neq \nu_c$

in calculations, is thus an artifice of the use of gradient models in representing physical processes which are not purely gradient in nature.

For the purposes of the present study we take two particular gradient models as representative of closure models for scalar transport. The first is that derived by assuming (3) and (8), i.e., the physically correct form of $\overline{u_i c}$ if gradient transport were truly the only mechanism causing transport. This is, in effect, a truncation of the exact Lagrangian expansion for the transport correlation. Its use in the subsequent comparisons helps clarify the extent to which transport models need to include the complete set of physical processes causing transport. To implement the use of (8), the necessary values of $\overline{u_i u_j}$ and the scales T_{ij} are obtained from direct numerical simulations of the flow field.

The second model[2,15] we consider is derived from an algebraic analysis of the transport equation for $\overline{u_i c}$. In this it is assumed that the sum of the scalar flux production terms in its own transport equation are aligned in the direction of the flux vector. From this an algebraic system of equations for $\overline{u_i c}$ follows whose solution fits the gradient form (3) with tensor eddy diffusivity given by

$$K_{ij} = \frac{1}{2A}\epsilon_{pki}\epsilon_{lmn}A_{lp}A_{mk}\overline{u_n u_j} \tag{14}$$

where A is the determinant of the matrix $A_{ij} = C_D/T\delta_{ij} + \partial\overline{U}_i/\partial x_j$,

$$C_D \equiv 16.1\left(1+\frac{1.17}{Sc}\right)^{.152}\left(1+\frac{131}{\sqrt{R_T}}\right)^{-.535}, \tag{15}$$

and the turbulent Reynolds number, $R_T \equiv 4k^2/\epsilon\nu$. Note that an alternative formula for C_D given in reference 2 gives virtually identical results to (15) in numerical applications and is thus not considered here. T is an appropriate time scale, essentially equivalent to that discussed previously in reference to (11). There are some important similarities between (8) and (14) which will become more evident below when we look at their forms in the particular flows to be considered.

III. UNIFORM SOURCE FLOW FIELD

We now consider the prediction of the mean scalar field due to a steady uniform source in the channel. In this case $\overline{C}(y)$ is one-dimensional and satisfies

$$0 = \frac{1}{ReSc}\frac{d^2\overline{C}}{dy^2} - \frac{d\overline{vc}}{dy} + \frac{2}{ReSc}, \tag{16}$$

where we have set $y = x_2$ and $v = u_2$. The arbitrary constant magnitude of the source in (16) is set to match the value used in previous studies[2,15–17]. For these conditions (8) becomes

$$\overline{vc} = -T_{22}\overline{v^2}\frac{d\overline{C}}{dy} \tag{17}$$

while the algebraic model (14) gives

$$\overline{vc} = -\frac{2k}{\epsilon}\frac{1}{C_D}\overline{v^2}\frac{d\overline{C}}{dy} \tag{18}$$

showing the close similarity between the two formulations of K_{ij} in this instance. In view of (17) it is clear that (18) contains the implicit assumption that

$$T_{22} = \frac{2k}{\epsilon}\frac{1}{C_D}, \tag{19}$$

which is, apart from the additional factor C_D, the standard scaling of the Lagrangian integral scale used in turbulence modeling.

We have performed a direct numerical simulation of the uniform source flow field from which the scalar mean and flux correlations are extracted for comparison with model predictions. This also provides values of $\overline{v^2}$, k, ϵ and T_{22} appearing in (17) and (18). The simulations incorporate a mesh with $64 \times 65 \times 64$ points in the streamwise, wall-normal and spanwise directions, respectively, and the dimensions of the computational box are $1250 \times 250 \times 625$ expressed in wall units. The numerical scheme is equivalent to that used in previous studies and is described in detail by Handler et al.[28]. The Reynolds number $R_\tau = U_\tau h/\nu = 125$, where U_τ is the friction velocity and h is the channel halfwidth, and $Sc = .71$. The $\overline{C}$ and $\overline{U}$ fields, Reynolds stresses, $\overline{u_i u_j}$, and transport correlations, $\overline{u_i c}$, agree closely with those found in previous studies[2,15–17].

From the simulated velocity field the time scale T_{22} was computed by first generating large ensembles of fluid particles arriving at fixed distances above the wall. To get highly accurate paths, velocities of the fluid particles at off nodal points were found by cubic hermite interpolation[29]. The estimates of T_{22} are limited to the range $0 \leq y^+ \leq 40$, so that it was necessary to extrapolate T_{22} to the centerline to get the complete curve for T_{22} needed in solving (16) using (17). Figure 1 shows the computed values of T_{22}, given in wall units, i.e., scaled by ν/U_τ^2, together with the approximate form used in (17). The latter consists of a least square fit in the region where the data is available, and its extension via a parabola to the 'ideal' value of T_{22} at the centerline. By 'ideal', we refer to the hypothetical magnitude that T_{22} would have at a point if the gradient model were locally exact there. This

distribution of T_{22} is also shown in the figure, as well as that given by (19). Near the wall the ideal form of T_{22} is significantly different from that computed from the DNS, suggesting that other physical effects besides gradient transport influence the $\overline{vc}$ correlation in this region. Further from the wall, the agreement becomes closer suggesting that a gradient model may have some legitimacy away from the boundary. It is noteworthy that (19) agrees closely with the ideal T_{22} for a sizable part of the channel, though they diverge near the centerline and near the wall, where the former goes to zero. The latter difference is largely immaterial to the performance of (19), however, since the appearance of $\overline{v^2}$ in the eddy diffusivity assures that the molecular diffusion coefficient will dominate (18) near the wall.

Random flight models discussed by Thomson[4,6] and von Dop et al.[5] were investigated here. For the uniform source channel flow $\overline{C}$ is one-dimensional so that only diffusion in the wall-normal direction need be considered. To implement the models, tracers were released into the flow at each time step from 40 uniformly spaced locations spanning the channel. The zero boundary condition was enforced by eliminating particles moving outside the domain. The number of tracers in the calculation grew to a statistically steady state, after which time the instantaneous C field was computed at every tenth time step over a time period of $t^+ = 5,000$, where $\Delta t^+ = 1$. The ensemble of these realizations were averaged to obtain a prediction of $\overline{C}$. At equilibrium, approximately 58,000 tracers were contained in the calculation.

We consider two random flight models. In the first, advancement of tracer position, y^n, and velocity, v^n, from time step $n\Delta t$ to $(n+1)\Delta t$ is through the rules

$$y^{n+1} = y^n + v^n \Delta t + \xi \tag{20}$$

and

$$v^{n+1} = v^n \left(1 - \frac{\Delta t}{T_{22}^{n+1}}\right) + \mu^{n+1}, \tag{21}$$

where ξ is a normally distributed random variable with mean 0 and variance $2\Delta t/ReSc$, i.e., $\xi = N(0, 2\Delta t/ReSc)$. The inclusion of this random change in position is necessary to accommodate molecular diffusion of the scalar. μ is also a random variable, though it is not necessarily Gaussian. For diffusion in non-homogeneous conditions, necessary values for its moments have been derived by Thomson[4]. These show that μ would be Gaussian – to first order in Δt – if both v were Gaussian and the condition $T_{22}(d\overline{v^2}/dy)/\overline{v^2} << 1$ were satisfied. In the present case, however, neither of these requirements are met, so it is unlikely that μ should be Gaussian. In generating μ for practical applications it is only possible to force a few of its moments to their correct values, so a degree of arbitrariness in the selection of μ

is to be expected.

According to the well-mixed criterion of Thomson[4], the mean, $\overline{\mu}$, variance, σ^2 and skewness, S_k, of μ should be, $\overline{\mu} = \Delta t \frac{d\overline{v^2}}{dy}$, $\sigma^2 = 2\Delta t\overline{v^2}/T_{22} + \Delta t \frac{d\overline{v^3}}{dy}$ and $S_k = 3\Delta t\overline{v^3}/T_{22} + \Delta t \frac{d\overline{v^4}}{dy} - \Delta t\overline{v^3}/\overline{v^2}\frac{d\overline{v^2}}{dy}$. In our implementation of (21) we took μ to be both Gaussian, in which case the first two moments are specified, and non-Gaussian, where μ was written as a sum of two Gaussian variables[4] in such a way as to meet the conditions on three moments. We also experimented with simplifications to the exact moment formulas. The most successful of the computations incorporated the non-Gaussian variable with the skewness simplified to $S_k = 3\Delta t\overline{v^3}/T_{22}$. The benefit of taking the skewness into account agrees with the earlier findings of Thomson for a test calculation under highly non-homogeneous conditions.

A second random flight approach consists of replacing (21) by the relation[4]:

$$v^{n+1} = v^n \left(1 - \frac{\Delta t}{T_{22}^{n+1}}\right) \frac{\sqrt{\overline{v^2}^{n+1}}}{\sqrt{\overline{v^2}^{n}}} + \mu^{n+1}. \tag{22}$$

In contrast to the previous algorithm, Gaussianity of v does imply that μ is Gaussian to $O(\Delta t)$, suggesting that there may be somewhat more justification for making μ Gaussian in this case. The computations showed, however, that various choices for μ, both Gaussian and non-Gaussian, gave relatively similar results. The best performance, though only marginally, came from specifying the first three moments according to $\overline{\mu} = \frac{\Delta t}{2} \frac{d\overline{v^2}}{dy}$, $\sigma^2 = 2\Delta t\overline{v^2}/T_{22} + \Delta t\overline{v^2}\frac{d(\overline{v^3}/\overline{v^2})}{dy}$ and $S_k = 3\Delta t\overline{v^3}/T_{22}$. In this case, the skewness has been abbreviated from its full expression, namely, $S_k = 3\Delta t\overline{v^3}/T_{22} + \Delta t\overline{v^2}^{3/2}\frac{d((\overline{v^4}-3\overline{v^2}^2)/\overline{v^2}^{3/2})}{dy}$.

The time scale in (21) and (22) is indicated as T_{22} since this choice is consistent with the premises upon which the random flight models are based. It should be noted, however, that neither this assumption nor the model itself are rigorously derived, so that it is conceivable that other choices for T_{22} may improve the performance of the models. Rather than consider such questions here, which are outside the scope of the present study, we took T_{22} as supplied from the direct numerical simulation. Since T_{22} is not precisely known for $y^+ \geq 40$, however, an attempt was made to explore the sensitivity of $\overline{C}$ to the mid-channel values of T_{22}. In this, the extrapolation of T_{22} to the center line was altered by up to 30%. This had a negligible effect on $\overline{C}$ suggesting that the present conclusions concerning the random flight models would not be significantly altered if more complete data for T_{22} were available.

Figure 2 compares $\overline{C}$ predicted from the closure models (17) and (18) against the solution determined from the direct numerical simulation. A similar comparison, but for the random flight models, is shown in FIG. 3. Evidently, despite whatever limitations there may be in the physical validity of gradient transport models, they are nonetheless quite adequate for

predicting this flow. The slightly greater accuracy of the algebraic model over (17) may be attributed to its time scale being lower than T_{22} in the region out to $y^+ = 20$. This leads to a higher slope in $\overline{C}$ near the wall and thus to a better fit further from the wall. Figure 3 shows that the scalar fields predicted by random flight models are generally less accurate than the closure models. The model based on (21) is more quantitatively correct than (22), though its shape is somewhat unphysical in appearance. The second model does capture the near wall field quite well, but seriously overpredicts $\overline{C}$ near the centerline. In view of the several orders of magnitude additional computational time needed in implementing the random flight methods in comparison to the transport models, it may be concluded that closure schemes represent a better choice for predicting one-dimensional diffusion under highly inhomogeneous conditions.

The total contribution to $\overline{vc}$ from non-gradient effects may be calculated by taking the difference between $\overline{vc}$ and (17). A plot of the resulting breakdown of $\overline{vc}$ is shown in FIG. 4 for the region where T_{22} is known. This has very much the same features[21] as a similar decomposition of the Reynolds shear stress $\overline{uv}$. In particular, gradient transport overpredicts $\overline{vc}$ near the wall and underpredicts it away from the wall. In view of the similarity of the $\overline{C}$ and $\overline{U}$ profiles, it is highly likely that this occurs for the same reasons as noted previously for momentum transport. In essence, a linear approximation to $\overline{C}$ near the wall overestimates the contribution to $\overline{v_a(\overline{C}_b - \overline{C}_a)}$ from particles traveling toward the wall, yet is reasonably accurate for particles traveling away from the wall. The result is an overprediction. Further from the wall the opposite occurs when the linear approximation is acceptable for those particles traveling wallward, yet underestimates the contribution of particles traveling outward, so that $\overline{v_a(\overline{C}_b - \overline{C}_a)}$ is underpredicted. Even though non-gradient effects contribute non-trivially to $\overline{vc}$, the flux is never counter-gradient so that the use of (17) cannot be ruled out as a model. Evidently, the success of (18) may be partly attributed to its beneficially modifying T_{22} to compensate for non-gradient physics in the uniform source flow.

Though the streamwise scalar flux $\overline{uc}$ does not appear explicitly in (16), it is nevertheless instructive to see how successfully this correlation can be modeled by the truncated Lagrangian and algebraic approaches. Here (8) gives

$$\overline{uc} = -\overline{uv}\, T_{12} \frac{\partial \overline{C}}{\partial y} \tag{23}$$

while (14) asserts that

$$\overline{uc} = -\left(\frac{T}{C_D} \overline{uv} - \frac{ST^2}{C_D^2} \overline{v^2} \right) \frac{\partial \overline{C}}{\partial y} \tag{24}$$

where $S = d\overline{U}/dy$ is the shear rate. Apart from the term depending on S in (24), one can view the algebraic model as implicitly modeling T_{12} by T/C_D, i.e., identical to the previous model for T_{22} implied by (18). A comparison of (23) and (24) versus the DNS solution is shown in FIG. 5. Values for T_{12} in (23) were computed from the simulation in very much the same way as T_{22} was calculated. Further discussion of these and other time scales will be presented below in the context of the plume flow field.

Both of the models (23) and (24) are in serious disagreement with the simulation results. The underprediction of $\overline{uc}$ by (24) is less than it would be if the shear term were not included, though closer agreement still would be had if the magnitude of T were increased. This can be justified, in fact, since T_{12} is much larger than T_{22} as will be seen below. This also helps explain why (23) very much overpredicts $\overline{uc}$ in comparison to (24). The prediction of $\overline{uc}$ from (23) follows a similar pattern as for $\overline{vc}$ in that it overpredicts near the wall and underpredicts away from it. Presumably this has the same physical explanation. Note that both gradient models are unphysical at the centerline where they each predict $\overline{uc}$ is zero, though the simulation suggests it is not. Evidently, streamwise transport near the centerline owes its presence to physical phenomena distinctly different from gradient transport. This is an interesting point which will be considered in future work.

IV. PLUMES

The simulation of plumes was carried out by equating Q in (1) to a Gaussian source term of the form

$$Q = \frac{100}{\pi} e^{-100(x^2+(y-y_o)^2)} \tag{25}$$

where the elevation of the source above the wall, y_o, was set to either $y_o^+ = 15$ or 30. For these calculations $R_\tau = 145$, the mesh contained $96 \times 97 \times 96$ points and the dimensions of the computational region were $1822 \times 290 \times 683$. The source was turned on at $t^+ = 0$ causing the subsequent plume to develop within a fully developed channel flow. Numerical values of $\overline{C}, \overline{uc}$ and $\overline{vc}$ as functions of x and y were obtained by averaging instantaneous realizations across the span. To get smoother statistics, many of the results presented below are the result of averaging over two independent realizations of the flow field.

It is in the nature of the developing plume that its mean properties reach steady state in an ever lengthening region extending downstream from the source. Beyond this domain the average plume properties are time dependent. Our subsequent interpretation of the computed scalar fields considers both steady and nonsteady aspects of the developing plumes.

Time accurate numerical schemes were used so that the modeled scalar fields could be meaningfully compared to the DNS field at any time after initiation of the plume. For the present study, comparisons are made generally at $t^+ = 87.5$.

Figure 6 shows the contours of $\overline{C}$ for the simulated plumes at $t^+ = 87.5$. For these and similar plots, the contour lines are in increments of unity. Contours of Q coming from (25) are superimposed so that the response of the plumes to source location may be observed. A significant difference between the two figures is the shift in the peak of $\overline{C}$ to a point on the wall surface when the plume source is brought from $y^+ = 30$ to 15. At $y^+ = 30$, the concentration peak in the near field remains immediately behind the center of the source, very much as it would be if the plume were developing in homogeneous turbulence in a uniform flow. The considerable differences between the plumes is due, in part, to the distributed nature of the source and the very much reduced convection and transport occurring at points close to the wall. The plume at $y^+ = 15$ is consistent with the expectation[30] that at points sufficiently far downstream of the source in the steady region, the peak concentration on a given cross section of the plume should lie at the wall. The steady region in the plume may be identified by the presence of contours ending approximately normal to the wall. According to FIG. 6a this extends to approximately $x^+ = 250$. For the $y^+ = 30$ plume the point where the maximum $\overline{C}$ at a fixed x is on the surface is much further downstream, beyond the limit of $x^+ = 600$ shown in the figure.

For a two-dimensional mean scalar field, the truncated Lagrangian expansion (8) yields

$$\overline{uc} = -\overline{u^2}\, T_{11}\frac{\partial \overline{C}}{\partial x} - \overline{uv}\, T_{12}\frac{\partial \overline{C}}{\partial y} \tag{26}$$

$$\overline{vc} = -\overline{uv}\, T_{21}\frac{\partial \overline{C}}{\partial x} - \overline{v^2}\, T_{22}\frac{\partial \overline{C}}{\partial y} \tag{27}$$

in which four distinct Lagrangian integral scales make an appearance. To utilize (26) and (27) as a model, the Reynolds stresses and time scales need to be supplied externally. In the present case these were obtained from the channel flow simulation at $R_\tau = 145$. Values of the scales at 10 positions between $y^+ = 0$ and $y^+ = 42$ were obtained from appropriate ensembles of backward particle paths computed over a time interval $t^+ = 43.8$. Least square fits to the scale values were computed for the region encompassing the scale data and these were extrapolated at constant value to cover the lateral extent over which the plumes spread during the time period $t^+ = 87.5$. Figure 7 shows approximate curves for all four scales together with the data points used in determining them. Note that the magnitude of T_{12} is very large near the wall, as was mentioned previously in reference to the evaluation of (23).

For those cases where the scales are of a magnitude close to or greater than 43.8, which applies generally to T_{11} and T_{12}, extrapolation of the partial integrals in (8) had to be used to estimate the scales, since the correlation functions were not yet zero. The curves in FIG. 7 are fully consistent with similar data acquired for the $R_\tau = 125$ simulation by Rovelstad[23]. For example, one may observe the close similarity between the T_{22} data in FIGS. 1 and 7.

For two-dimensional mean flows the algebraic model (14) predicts that

$$\overline{uc} = -\left(\frac{T}{C_D}\overline{u^2} - \frac{ST^2}{C_D^2}\overline{uv}\right)\frac{\partial \overline{C}}{\partial x} - \left(\frac{T}{C_D}\overline{uv} - \frac{ST^2}{C_D^2}\overline{v^2}\right)\frac{\partial \overline{C}}{\partial y} \tag{28}$$

$$\overline{vc} = -\left(\frac{T}{C_D}\overline{uv}\right)\frac{\partial \overline{C}}{\partial x} - \left(\frac{T}{C_D}\overline{v^2}\right)\frac{\partial \overline{C}}{\partial y} \tag{29}$$

where, as before, $T \equiv 2k/\epsilon$. When $S = 0$ these equations become equivalent to (26) and (27) under the assumption that all of the scales are equal to T/C_D. With this restriction, the algebraic approach is equivalent to previously developed models[31].

Numerical solutions to (2) containing either (26) and (27) or (28) and (29) were obtained using the ADI algorithm applied to second order differences of all spatially differentiated terms. The computational domain was taken to be $-200 \leq x^+ \leq 1800$ and $0 \leq y^+ \leq 150$. A uniform finite difference mesh was used with dimensions 1000×100 and $\Delta t^+ = .1$. Zero flux boundary conditions were imposed on all boundaries. The computed results were found to be independent of time and space discretization as well as domain size.

For the simulation of the plume using the random flight methodology, we used the multi-dimensional model of Thomson[6] which generalizes the second of the two one-dimensional models considered previously. In this case tracers are represented by their positions (x^n, y^n) and velocities (U^n, V^n). The mean and fluctuating velocities at the tracer locations are denoted by $(\overline{U}^n, \overline{V}^n)$ and (u^n, v^n), respectively. Particle positions are updated by the rules

$$x^{n+1} = x^n + (\overline{U}^n + u^n)\Delta t + \xi_1 \tag{30}$$

$$y^{n+1} = y^n + v^n \Delta t + \xi_2 \tag{31}$$

where (ξ_1, ξ_2) are mutually independent Gaussian random variable with means 0 and variances $2/ReSc$. Coupled to (30) – (31) are the relations

$$u^{n+1} = (1 - \frac{\Delta t}{T_{11}^{n+1}}u^* - \frac{\Delta t}{T_{12}^{n+1}}v^*) + \mu_1^{n+1} \tag{32}$$

$$v^{n+1} = (1 - \frac{\Delta t}{T_{21}^{n+1}}u^* - \frac{\Delta t}{T_{22}^{n+1}}v^*) + \mu_2^{n+1} \tag{33}$$

where (u^*, v^*) is computed on alternate time steps through the equations

$$\begin{pmatrix} u^* \\ v^* \end{pmatrix} = \begin{pmatrix} u^n \\ v^n \end{pmatrix} + \Delta t \begin{pmatrix} \frac{d\overline{uv}}{dy} \\ \frac{d\overline{v^2}}{dy} \end{pmatrix} \tag{34}$$

and

$$\begin{pmatrix} u^* \\ v^* \end{pmatrix} = \begin{pmatrix} \overline{u^2}^{n+1} & \overline{uv}^{n+1} \\ \overline{uv}^{n+1} & \overline{v^2}^{n+1} \end{pmatrix} \begin{pmatrix} \overline{u^2}^{n} & \overline{uv}^{n} \\ \overline{uv}^{n} & \overline{v^2}^{n} \end{pmatrix}^{-1} \begin{pmatrix} u^n \\ v^n \end{pmatrix}. \tag{35}$$

As discussed by Thomson[6], the random vector (μ_1, μ_2) is taken to be Gaussian with zero mean and covariance $\sigma_{ij} \equiv \overline{\mu_i \mu_j}$ given by

$$\sigma_{11} = 2(\frac{\Delta t}{T_{11}}\overline{u^2} + \frac{\Delta t}{T_{12}}\overline{uv}) \tag{36}$$

$$\sigma_{12} = \sigma_{21} = (\frac{\Delta t}{T_{11}} + \frac{\Delta t}{T_{22}})\overline{uv} + \frac{\Delta t}{T_{12}}\overline{u^2} + \frac{\Delta t}{T_{21}}\overline{v^2} \tag{37}$$

$$\sigma_{22} = 2\Delta t(\frac{\Delta t}{T_{22}}\overline{v^2} + \frac{\Delta t}{T_{21}}\overline{uv}). \tag{38}$$

Alternative choices for (μ_1, μ_2) involving conditions on the higher moments can be postulated as in the one-dimensional case, though the advantages of this strategy remain unclear at the present time. In fact, for the high shear environment of the current application, this may be detrimental[10].

As in the one-dimensional case considered previously, it is natural to equate the scales in (32), (33) and (36) – (38) with the equivalent Lagrangian integral scales. However, with these values for T_{22} and T_{21} a computation revealed that σ_{22} given by (38) would be negative near the wall due to the quotient of $\overline{uv}$, which is negative, and T_{21}, which is relatively small (see FIG. 7). To insure the positive definiteness of σ_{22}, the expediency was taken of dropping the $\overline{uv}$ terms from (36) and (38). An alternative strategy was also tried in which σ_{22} was made positive by replacing T_{21} by T_{12}. The difference in $\overline{C}$ between the two approaches was slight, suggesting that the influence of the $\overline{uv}$ term in (36) and (38) is not very significant. Clearly, however, future attention needs to be paid to clarifying the rationale behind the formulas given in (36) - (38).

Random variables with the specified covariances (36) – (38) were generated by computing two independent random variables $\eta_1 = N(0, (\sigma_{11} + \sigma_{22} + \Sigma)/2)$ and $\eta_2 = N(0, (\sigma_{11} + \sigma_{22} - \Sigma)/2)$ where $\Sigma \equiv \sqrt{(\sigma_{11} - \sigma_{22})^2 + 4\sigma_{12}^2}/2$, and then setting

$$\mu_1 = (\sigma_{12}\ \eta_1 - \frac{1}{2}(\sigma_{22} - \sigma_{11} + \Sigma)\ \eta_2)/D \tag{39}$$

$$\mu_2 = (\frac{1}{2}(\sigma_{22} - \sigma_{11} + \Sigma)\ \eta_1 + \sigma_{12}\ \eta_2)/D \tag{40}$$

where $D \equiv \sqrt{(\Sigma^2 + \Sigma(\sigma_{22} - \sigma_{11}))/2}$. To simulate the plume flow, tracer particles were released into the channel at each time step from a grid of locations covering the source: 200 in the case of the $y^+ = 15$ plume and 225 for the $y^+ = 30$ plume. The amount of scalar given to each tracer depended on the amplitude of Q at its initial location. The integration time step was $\Delta t^+ = .5$ and the plume was computed for 175 time steps representing an elapsed time of $t^+ = 87.5$. To get smooth statistics, the calculation was repeated 500 times and averaged. The independence of the algorithm to time step was tested by repeating the calculation with $\Delta t^+ = .35$ for 250 time time steps. The average statistics from this calculation could not be distinguished from the first.

Plots of the predicted plumes based on (26) – (29) and the random flight model are shown in FIGS. 8 – 10. Comparing these to the direct numerical simulation results in FIG. 6 gives insight into the qualitative performance of the models. It is noteworthy that the two closure models appear to successfully capture the shift of the peak in $\overline{C}$ to the wall surface for the $y^+ = 15$ plume. This trend is also partially captured by the random flight model in that the peak is shifted toward the wall, but is not quite on the surface.

By counting the number of contour lines in each figure, it may be concluded that the closure models tend to overpredict the peak in $\overline{C}$ for both plumes. A similar trend is observed for the random flight model at $y^+ = 30$, though the peak in the $y^+ = 15$ plume is underpredicted. All of the models slightly overpredict the downstream widening of the plume. Focusing on the downstream extent of the steady regime, i.e., the domain where the contours are normal to the boundary, it may be seen in FIGS. 8a – 10a that the closure models are qualitatively correct in this regard while the random flight model fails to capture the trend. In fact, the random flight solution at $y^+ = 15$ does not show an adequate response to the presence of the wall, having similar characteristics as the $y^+ = 30$ plume. All of the models are better at predicting the structure of the $y^+ = 30$ plume than the $y^+ = 15$ plume, presumably because the turbulence is more homogeneous away from the wall so that less of a demand is placed on the modeling.

The expectation that the random flight model should be better at capturing the near field dispersion than gradient models is well borne out, at least qualitatively, by the current results. Among the plumes depicted in FIGS. 8 - 10, the random flight model is clearly superior in capturing the correct trends in $\overline{C}$ near the source. This is quite apparent in FIGS. 6a and 10a. The equivalent regions in FIG. 8a and 9a are qualitatively different in that the upstream spread of $\overline{C}$ is overpredicted leading to an unphysical distortion of the

plume. A similar exaggerated upstream dispersion may be seen in the case of the $y^+ = 30$ plume.

The near field errors associated with the closure models may be attributed to a fundamental failure of (26) and (28) to accurately represent $\overline{uc}$ near the source. In particular, FIG. 11 is a plot of the DNS prediction of $\overline{uc}$ on a streamwise cut at $y^+ = 15$ through the $y^+ = 15$ plume, together with evaluations of (26) and (28) using the $\overline{C}$ field computed from the DNS solution. The latter are the values $\overline{uc}$ would have if the models had yielded the correct $\overline{C}$ field. It is seen that $\overline{uc}$ is negligible upstream of $x^+ = -20$, becomes negative through the source region and then slowly rises into the steady part of the plume. In contrast, equations (26) and (28) predict a large negative spike in $\overline{uc}$ near the origin of the plume. This behavior is attributable to the dependence of (26) and (28) on $\frac{\partial \overline{C}}{\partial x}$, which is large and positive at the source of the plume. Since T_{11} is much larger than T/C_D, (26) is less accurate than (28) and the plume in FIG. 8a spreads further upstream than that in FIG. 9a. Note that in this situation the shear term in (28) does not act to improve the prediction of $\overline{C}$ as it did in the case of the uniform source. Downstream of the source, (26) and (28) quickly relax to slowly varying negative values resulting from the contribution of their respective terms containing $\frac{\partial \overline{C}}{\partial y}$. For the truncated Lagrangian model in (26) this agrees closely with the correct value suggesting that $\overline{uc}$ may very well be describable by gradient transport far enough downstream of the source. Note that the greater accuracy of (26) over (28) in this instance must stem from the use of the physical time scales rather than the model T/C_D. In particular, if gradient transport were the only significant process present in the flow, then (26) would have to be more accurate than (28).

A quantitative view of the accuracy of the models is given in FIGS. 12 - 15 showing the computed $\overline{C}$ fields on x and y coordinate lines intersecting the plumes. Figures 12 and 13 are cuts in the streamwise direction at the level of the centers of the sources at $y^+ = 15$ and 30, respectively. The scalar field distribution across the $y^+ = 15$ plume at $x^+ = 100$ and 500 is shown in FIGS. 14a and 14b, and a similar plot for the $y^+ = 30$ plume is shown in FIGS. 15a and 15b. The line $x^+ = 100$ is relatively close to the source, where the plume has reached steady state, while $x^+ = 500$ is away from the immediate sphere of influence of the source in the region which is still developing at $t^+ = 87.5$. According to FIGS. 12 and 13, the closure models achieve considerable quantitative accuracy downstream of the source, in fact, reproducing the general trends quite well. Only in the near field is the accuracy seriously degraded by overprediction brought on by the unphysical upstream diffusion caused by the gradient models. This does not appear to affect the downstream solution too seriously. The

near field errors are noticeably less for the $y^+ = 30$ plume presumably because the greater convection velocity of the flow counteracts the errors in $\overline{uc}$.

The quantitative accuracy of the random flight model appears to be significantly below that of the closure models. It substantially overpredicts the plume magnitude near the source in both cases, while in the far field it underpredicts the $y^+ = 15$ plume yet overpredicts the $y^+ = 30$ plume. The principal strength of the method is in capturing the distribution of $\overline{C}$ at the upstream end of the plumes. This aspect of the mean scalar field is clearly superior to that deriving from the closure schemes.

The mean scalar profiles for the cross-stream slice shown in FIG. 14a reveals that the closure models are relatively successful in capturing the complete trend of the plume in the steady region. The accuracy is fairly well maintained into the nonsteady region as well, as seen in FIG. 14b. For the $y^+ = 30$ plume in FIG. 15a, similar results are obtained, though there is a slight overprediction in the lateral spreading and the errors near the wall become fairly pronounced downstream, as seen in FIG. 15b. The plots of $\overline{C}$ for the random flight model bring into sharper focus the difficulty faced by this method in correctly perceiving the influence of the boundary. As seen in FIG. 14a, reasonable accuracy is achieved only for $y^+ > 20$, while the behavior adjacent to the wall is clearly unsatisfactory. For the $y^+ = 30$ plume, the difficulty in resolving the wall influence becomes quite noticeable in FIG. 15b at $x^+ = 500$ where the plume is now in contact with the wall. At $x^+ = 100$, before the wall effect is significant, the trend of $\overline{C}$ is well represented, apart from the peak which is too high.

We have previously considered the suitability of gradient modeling of $\overline{uc}$ in the near and far field of the plume, and we now consider the same question for the lateral transport correlation $\overline{vc}$. Figure 16 compares $\overline{vc}$ from the DNS with (27) and (29) evaluated using the correct $\overline{C}$ field, at cuts across the $y^+ = 30$ plume at 100 and 300. Significant errors in the gradient models are evident at $x^+ = 100$ in FIG. 16a but not in FIG. 16b at $x^+ = 300$. At the first of these locations fluid particles are within an integral time scale of the origin, so the gradient model should be of questionable validity, as first predicted by the classical analysis of Taylor[8]. The second position belongs to the approximately steady region downstream of the near field where gradient transport has a greater likelihood of being legitimate. Evidently, FIG. 16b does not contradict this supposition. In the next section we will discuss in greater detail the physical mechanisms behind these properties of $\overline{vc}$.

The quantitative differences between the scalar fields and fluxes predicted by the two closure models are almost entirely due to the different values used for the scales. In particular, the influence on $\overline{C}$ of the terms depending on S in (28) is relatively small. In fact, an

independent calculation of the plume using (28) and (29) in which S was set to zero, revealed a change in $\overline{C}$ of generally less than one percent. This appears to be a consequence of the fact that beyond the initial region, the model for $\overline{vc}$ – which according to (29) has no dependence on shear – is the dominant turbulent influence on the plume. It may be concluded that the success of gradient models in predicting the far field of homogeneous turbulence also extends to the non-homogeneous case as well, so long as they include the basic dependence on Reynolds stress exhibited by (26) and (27) or (28) and (29). The use of physically accurate scales improves the predictions of the far field fluxes at the expense of greater errors in the near field, while the opposite happens if the modeled scales are used. Both strategies give comparable predictions of the mean scalar field.

V. TRANSPORT PHYSICS

Our previous results suggest that improvements to the modeling of the turbulent flux rate in the near field of plumes is essential if progress is to be made in predicting contaminant dispersal through the Reynolds averaged formulation. Errors made by gradient models near sources affect not only the near field, but must inevitably translate into inaccuracies further downstream, even where gradient transport may have a degree of legitimacy. The Lagrangian methodology presented earlier provides a systematic means for exploring the physics of the flux correlation. In the following we adopt this approach toward illuminating the physical processes responsible for scalar transport, including an analysis of how and where the changeover to gradient physics takes place along the plume. The analysis given here will cover only some of the principal aspects of the $\overline{vc}$ correlation. We leave a more comprehensive treatment to a subsequent study in which the influence of coherent vortical structures is also taken into account.

The physics of the scalar flux in the near field of a turbulent plume was first considered by Taylor[8] who showed that the lateral growth rate of a plume near its source is incompatible with the $\sqrt{t}$ growth implied by a diffusion equation. In particular, for flight times less than the local Lagrangian integral scale, the random positions of fluid particles initially at the source, cannot be accurately described as having undergone a sum of independent random steps. Instead, their initial motion persists over a time on the order of the integral time scale, leading to a lateral growth rate in the plume proportional to t. Through various devices[30,32] it has been argued that a gradient law modified to admit space or time dependent eddy diffusivities may account for the near field flux rate. These lack rigorous justification,

however, and are subject to a number of conceptual difficulties, including the assumption that the eddy diffusivity is a property of the plume and not exclusively of the underlying turbulent flow. For plumes with countergradient transport in the near field[7], such models may be *a priori* disqualified. After we formally apply our transport analysis, it will become still more evident that the physics of the near field has little to do with the gradient transport mechanism, even if modified by a variable eddy diffusivity.

Our analysis of $\overline{vc}$ proceeds by evaluating the terms in the Lagrangian decomposition (4) and (5) applied to the plume flow. We specifically consider the $y^+ = 15$ plume at a series of points arrayed along the line $y^+ = 30$. These intersect the region of peak $\overline{vc}$ as may be seen in FIG. 17 where the positive contours of $\overline{vc}$ are plotted together with the points where the Lagrangian decomposition is evaluated. Note that $\overline{vc}$ is positive on the side of the plume facing away from the wall in accordance with the expected direction of the turbulent flux. To evaluate (4) and (5), ensembles of 200 particles paths each were computed with termination points distributed uniformly across the span at each of the points in FIG. 17. A second ensemble at each point was obtained using a later realization of the flow field so as to enhance the smoothness of the statistics.

It is a property of the plume flow that fluid particles upstream of the source must necessarily have $C = 0$. Since we have defined the mixing time at a point a as the earliest time at which $\overline{v_a c_b} \approx 0$, τ_m must always be smaller than the minimum time needed for the fluid particles in an ensemble to travel from positions b upstream of the plume origin to a. In particular, for such a time interval $C_b = \overline{C}_b = c_b = 0$ so certainly $\overline{v_a c_b} = 0$. For final positions near the source, the backward fluid particle paths must have been upstream of it a short time earlier, and it can be expected that $\overline{v_a c_b}$ will be zero for relatively short τ. It is thus evident that the mixing time must be small for points near the source, and progressively increase downstream. For distances far enough downstream, it is likely that $\overline{v_a c_b}$ would be zero for a time τ before all the fluid particles in an ensemble could be located upstream of the source. This must occur since some of the particles are entrained into the plume and therefore have $C_b = 0$, while for others the natural decorrelation caused by the random motion must exert an influence. It is thus clear that τ_m should approach an equilibrium value at points sufficiently far from the source.

Figure 18 shows the dependence of mixing time, computed here as the time where $\overline{v_a c_b}$ is within 5% of zero, on the distance downstream of the source. It is seen to rise linearly until $x^+ \approx 120$, after which it shows a tendency to level off to a value near $\tau_m^+ \approx 18$. For the uniform source flow considered in the previous section, a calculation gives $\tau_m^+ = 16$ at

$y^+ = 30$. The similarity of this value to the asymptote in FIG. 18 is not unexpected, since in the far field of the plume, mixing is achieved largely within the plume itself by a mechanism which is presumably similar to that occurring in the uniform source flow.

For any $\tau > \tau_m$, the physical processes underlying the scalar flux are given by the second two terms in (4). We now consider the behavior of this decomposition as a function of τ for the first and last points indicated in FIG. 17, i.e., at the locations $x^+ = 20$ and 160. These curves, scaled by $\overline{v_a c_a}$, are given in FIG. 19 where it should be noted that the abscissa is τ, i.e., the time interval over which fluid particles are tracked. Small τ means the points b are close to the final point a while large τ means they are significantly upstream of a. As seen previously in FIG. 18, FIG. 19a indicates that the mixing time is very small at $x^+ = 20$, in fact, $\overline{v_a c_b} \approx 0$ by $t^+ = 5$. Since $x^+ = 20$ is near the source, evidently all of the fluid particles in the ensemble are upstream of it for $\tau^+ = 5$. It may also be noticed in FIG. 19a that $\overline{v_a(C_a - C_b)}$ is slightly negative for small τ and then approaches $\overline{v_a c_a}$ when τ is on the order of τ_m.

An essential aspect of FIG. 19a is that the displacement transport term is zero when the mixing time is first reached. It is not uniformly zero throughout the interval, however, as is seen by its rise to a positive peak before dropping to zero just when mixing occurs. The eventual drop off to zero is a necessary consequence of the fact that $\overline{v_a \overline{C_a}} \equiv 0$ and $\overline{v_a \overline{C_b}} \to 0$ as $\tau \to \infty$. It is evident from these observations that while some of the physical mechanisms associated with displacement transport are active in the flow near the source, these cannot usefully be incorporated into a transport model because they occur only while v_a and c_b are still significantly correlated. Previous analyses[21,24] have shown that displacement transport is a phenomenon operating on the time scale over which vortices exert a significant influence on fluid particle displacement. Consequently, it is not surprising that a short mixing time is incompatible with displacement transport. Further downstream in the plume, where the mixing time is larger, there should be no such prohibition. The conclusion may be reached from this interpretation of FIG. 19a that in the near field of the source it is most appropriate to view $\overline{vc}$ as being due entirely to the correlation $\overline{v_a(C_a - C_b)}$, i.e., that $\overline{vc}$ results from the two processes indicated in (5).

The dependence of the terms in (4) on τ have a distinctly different character at locations further from the source, such as at $x^+ = 160$, shown in FIG. 19b. τ_m is much larger here, on the order of $15 - 20$, and the displacement transport term may be seen to have developed the beginning of a plateau near its maximum value. Most importantly, the plateau occurs only after $\overline{v_a c_b}$ has become relatively small, i.e., after mixing has occurred. Similarly,

there is also a suggestion of a plateau in $\overline{v_a(C_a - C_b)}$, when $\tau \approx \tau_m$, though the noise produced by the relatively small number of fluid particles in the sample makes it difficult to be definitive in this regard. For $\tau^+ \approx 12$ the pattern discussed previously in reference to FIG 19a rapidly reappears when the fluid particles in the ensemble are all upstream of the source. The decomposition of $\overline{vc}$ in FIG 19b is potentially useful for any $\tau > \tau_m$, but clearly the most physically beneficial result is when $\tau \approx \tau_m$. From this perspective, it is evident that displacement transport represents a dominant effect in the creation of the $\overline{vc}$ correlation at $x^+ = 160$.

To gain an idea of where the changeover takes place from the near field physics of $\overline{vc}$, as exemplified by FIG. 19a, to that more in keeping with the far field shown in FIG. 19b, we plot the displacement transport terms in FIG. 20 for a number of x^+ positions further and further from the source. The growth and development of a plateau in $\overline{v_a(\overline{C}_b - \overline{C}_a)}$ is observed as well as a leveling off in the peak. This suggests that displacement transport emerges as the most significant transport mechanism at the distance of $x^+ \approx 150$ from the plume origin. Between $x^+ = 20$ and this location, a transition between the two mechanisms takes place. At points further downstream than $x^+ = 160$, the plateau region should occupy an ever longer time interval.

While the displacement term becomes dominant in the neighborhood of $x^+ = 150$, it does not necessarily follow that gradient transport is an accurate representation of this process. In fact, since $\overline{C}$ varies quite considerably in the near field of the plume, and fluid particles arriving near $x^+ = 150$ traverse this region during the mixing time, dependence of the displacement term on the mean scalar gradient at a single point seems unlikely. This is supported by the fact that T_{22} appearing in $-T_{22}\overline{v^2}d\overline{C}/dy$ is approximately 10 (see FIG. 7), i.e., on the order of the mixing time. Only further downstream is it likely that fluid particles will travel through a relatively uniform part of the plume during τ_m so that the gradient relation may be more approximately valid.

Our consideration of FIG. 19a showed that the physics of the lateral scalar flux near the plume can be expressed as

$$\overline{v_a c_a} = \overline{v_a(C_a - C_b)} = \frac{1}{ReSc}\int_{-\tau}^{0} \overline{v_a \nabla^2 C(s)}ds + \int_{-\tau}^{0} \overline{v_a Q(s)}ds \qquad (41)$$

as long as $\tau > \tau_m$. The relative importance of each of the terms in (41) can be expected to depend on position in the plume. For the point at $x^+ = 20, y^+ = 30$ in FIG. 17, a breakdown of $\overline{v_a(C_a - C_b)}$ according to (41) is given in FIG. 21. This reveals that $\overline{vc}$ is due mostly to the second term, i.e., that v is correlated with the cumulative scalar acquired by fluid particles as they meander through the source. The overprediction of $\overline{vc}$ by this term is balanced by

a negative contribution from the first term in (41), suggesting that there is a correlation between v and the gain or loss of scalar by molecular diffusion.

To better understand the result in FIG. 21, we show the individual contributions made by the 400 particles in our ensemble at $x^+ = 20$, to the integral terms in (41). The abscissa gives the initial y^+ locations of the fluid particles and the ordinate gives either the magnitude of $\frac{1}{ReSc}\int_{-\tau}^{0} v_a \nabla^2 C(s)ds$ (+ symbol) or $\int_{-\tau}^{0} v_a Q(s)ds$ (o symbol) for each particle. Since all of the fluid particles arrive at $y^+ = 30$, those beginning below this level generally have $v_a > 0$, while those starting above ordinarily have $v_a < 0$. A number of important conclusions can be drawn from the figure. In the first place, very few particles gain or lose significant amounts of scalar by molecular diffusion, as we anticipated from FIG. 21, and those that do are seen to be traveling from below $y^+ = 30$ contributing negatively to $\frac{1}{ReSc}\int_{-\tau}^{0} v_a \nabla^2 C(s)ds$. This suggests that $\nabla^2 C(s) < 0$ for these particles and they are losing scalar as they travel. According to FIG. 21, $\int_{-\tau}^{0} \overline{v_a Q(s)}ds$ is zero for small τ while $\frac{1}{ReSc}\int_{-\tau}^{0} \overline{v_a \nabla^2 C(s)}ds < 0$, so the latter term is fully responsible for the slight negative region of $\overline{v_a(C_a - C_b)}$. The conclusion follows that the negative contribution to $\overline{vc}$ from the first term in (41) arises from fluid particles systematically losing scalar by molecular diffusion after leaving the vicinity of the source.

Figure 22 shows that virtually all of the fluid particles in the ensemble make a non-zero contribution to $\overline{vc}$ via the mechanism represented by the second term in (41). This is not unexpected in view of the proximity of the point $x^+ = 20, y^+ = 30$ to the source, as seen in FIG. 6. The individual contributions to $\int_{-\tau}^{0} v_a Q(s)ds$ add up to a net positive flux, since fluid particles traveling away from the wall ($v_a > 0$) pass through both a greater portion of the source and its most intense part, in contrast to fluid particles heading toward the wall. This is also evident in the lack of symmetry of the individual contributions to $\int_{-\tau}^{0} v_a Q(s)ds$ about the line $y^+ = 30$ displayed in FIG. 22. Note that the largest positive contributions come from a relatively small number of particles traveling from much closer to the wall. Presumably these are associated with ejections of low speed fluid which are a major factor in the dynamics of the flow in the vicinity of $y^+ = 30$.

We see from these considerations that scalar transport in the near field of the source reflects an interaction between the contaminant as it is released into the fluid and the underlying turbulent eddying motion. This process has little connection to the mechanisms ordinarily associated with gradient transport. Allowing the eddy diffusivity to have plume dependent properties also does not come closer to modeling the correct physics. At distances progressively further downstream from the plume origin, the correlation between v and the

scalar acquired at the source by fluid particles diminishes while displacement transport becomes the dominant source of the turbulent scalar flux.

VI. CONCLUSIONS

The performance of random flight and closure models in predicting scalar transport has been examined under the controlled conditions offered by a direct numerical simulation of turbulent channel flow with uniform and line sources. It is evident that under the highly anisotropic and inhomogeneous conditions of the channel, closure models provide substantially better quantitative accuracy than random flight models at a reduced computational cost. The range of applications of closure models in the gradient form is limited, however, by their failure to accommodate the near field of plumes. Though random flight models provide greater realism in modeling near the plume source, they are prone to substantial errors in the mean scalar field and do not appear to well accommodate the presence of solid boundaries in multi-dimensional flow.

The mathematical structure of the gradient model given in (26) and (27) or (28) and (29) proved to be adequate for modeling the steady far field of plumes. Since the shear terms in (28) had very little effect on predictions, the most important issue in the development of gradient models is the choice of time scales. The use of the theoretically derived Lagrangian integral scales has the advantage of being more accurate in the far field of the plume, though this is gained only at the expense of a significant distortion in the near field. Through its use of simplified scales, the algebraic model reduces the errors in the near field, but is then somewhat less accurate in representing transport in the far field. For the predicted scalar fields, however, both alternatives are found to have comparable accuracy. Implementation of (28) and (29) in applications may be easier than (26) and (27) since it may be problematical to obtain values of the four Lagrangian integral scales under general flow conditions. In both cases, the Reynolds stresses need to be available, and for the algebraic model, k and ϵ, as well. Such quantities must generally be acquired from closure schemes which are prone to considerable errors themselves. Consequently, the practical implementation of the scalar flux models will often be prone to additional errors which are unrelated to their form.

For the significant inhomogeneities present in channel flow, the random flight models, as they currently are constructed, do not appear to be adequate. While the necessary moment conditions for the one-dimensional model are known, the need to simplify these requirements appears to severely degrade the resulting predictions. For the two-dimensional calculations,

the moment conditions are in need of more development, particularly where the flow is most inhomogeneous near walls. Clearly, if such methods are to be a source of accurate predictions of scalar diffusion in the near field of plumes developing within inhomogeneous turbulent flows, they must undergo some significant modifications.

A high priority in improving the accuracy of predictions based on turbulent scalar transport models must lie in increasing their range of applicability to include the near field of plumes. As a step toward this end, we have made a limited application of the Lagrangian methodology to the lateral transport correlation at various points where it is at a local peak. This showed in some detail why gradient transport is unlikely to be a significant factor in the near field of plumes. In particular, the mixing time is too small for displacement transport to fully create a correlation between v and c. Further downstream, where fluid particles spend much longer times within the plume, the physical mechanisms behind the scalar flux shift to that of displacement transport which may be reasonably well modeled via a gradient term. In the near field $\overline{vc}$ represents mostly the average effect of the turbulent flow meandering over the source. This is slightly offset by an effective transport caused by fluid particles systematically losing scalar by molecular diffusion after leaving the source. The prediction of scalar fields in inhomogeneous turbulence should be considerably advanced once models of these fundamental processes are developed.

REFERENCES

[1]A. Yoshizawa, "Statistical modeling of passive scalar diffusion in turbulent shear flows," J. Fluid Mech., **195**, 541 (1988).

[2]M. M. Rogers, N. N. Mansour, and W. C. Reynolds, "An algebraic model for the turbulent flux of a passive scalar," J. Fluid Mech., **203**, 77 (1989).

[3]K. Horiuti, "Assessment of two-equation models of turbulent passive scalar diffusion in channel flow," J. Fluid Mech., **238**, 405 (1992).

[4]D. J. Thomson, "Random walk modeling of diffusion in inhomogeneous turbulence," Quart. J. Roy. Met. Soc., **110**, 1107 (1984).

[5]H. van Dop, F. T. M. Nieuwstadt, and J. C. R. Hunt, "Random walk models for particle displacements in inhomogeneous unsteady turbulent flows," Phys. Fluids, **28**, 1639 (1985).

[6]D. J. Thomson, "A random walk model of dispersion in turbulent flows and its application to dispersion in a valley," Quart. J. Roy. Met. Soc., **112**, 511 (1986).

[7]M. R. Raupach, "A practical Lagrangian method for relating scalar concentrations to source distributions in vegetation canopies," Quart. J. Royal Met. Soc., **115**, 609 (1989).

[8]G. I. Taylor, "Diffusion by continuous movements," Proc. London Math. Soc. **XX**, 196 (1921).

[9]C. A. Degrazia and O. L. L. Moraes, "A model for eddy diffusivity in a stable boundary layer," Boundary Layer Met., **58**, 205 (1991).

[10]T. K. Flesch and J. D. Wilson, "A two-dimensional trajectory-simulation model for non-Gaussian, inhomogeneous turbulence within plant canopies," Boundary Layer Met., **61**, 349 (1992).

[11]H. Van Dop, "Buoyant plume rise in a Lagrangian framework," Atmos. Env., **26**, 1335 (1992).

[12]Y. Shao, "Turbulent dispersion in coastal atmospheric boundary layers: an application of a Lagrangian model," Bound. Layer Met., **59**, 363 (1992).

[13]J. M. Macinnes and F. V. Bracco, "Stochastic particle dispersion modeling and the tracer-particle limit," Physics Fluids A, **4**, 2809 (1992).

[14]D. J. Thomson, "Criteria for the selection of stochastic models of particle trajectories in turbulent flows," J. Fluid Mech. **180**, 529 (1987).

[15]W. C. Reynolds, M. M. Rogers & N. D. Sandham, "Advances in turbulent transport modeling based on direct simulations of turbulence," *Transport Phenomena in Turbulent Flows: Theory, Experiment, and Numerical Simulation*, edited by M. Hirata, N. Kasagi, (Hemisphere, N. Y., 1988), pp. 701 - 713.

[16]J. Kim and P. Moin, "Transport of passive scalars in a turbulent channel flow," in *Turbulent Shear Flows 6*, edited by J.-C. Andre et al., (Springer, N. Y., 1987) pp. 5-2-1 - 5-2-8.

[17]J. Kim, "Investigation of heat and momentum transport in turbulent flows via numerical simulations," *Transport Phenomena in Turbulent Flows: Theory, Experiment, and Numerical Simulation* edited by M. Hirata, N. Kasagi, (Hemisphere, N. Y., 1988), pp. 715 - 729.

[18]N. Kasagi and Y. Ohtsubo, "Direct numerical simulation of passive scalar field in a turbulent channel flow," ASME J. Fluids Engrg., **114**, 598 (1992).

[19]P. K. Yeung, J. G. Brasseur and D. M. Bell, "Evolution of passive scalar sources in a numerically simulated boundary layer," in *Near Wall Turbulent Flows*, edited by R. M. C. So, C. G. Speziale and B. E. Launder, (Elsevier, Amsterdam, 1993), pp. 307 - 316.

[20]D. M. Bell and J. H. Ferziger, "Turbulent boundary layer DNS with passive scalars," in *Near Wall Turbulent Flows*, edited by R. M. C. So, C. G. Speziale and B. E. Launder,

(Elsevier, Amsterdam, 1993), pp. 327 - 336.

[21]P. S. Bernard and R. A. Handler, "Reynolds stress and the physics of turbulent momentum transport," J. Fluid Mech., **220**, 99 (1990).

[22]P. S. Bernard, "Turbulent vorticity transport in three dimensions," *Theor. Comput. Fluid Dyn.*, **2**, 165, (1990).

[23]A. Rovelstad, "Lagrangian analysis of vorticity transport in a numerically simulated turbulent channel flow," Ph. D. Thesis, Univ. of Maryland, College Park, (1991).

[24] P. S. Bernard, J. M. Thomas and R. A. Handler, "Vortex dynamics and the production of Reynolds stress," J. Fluid Mech., **253**, 385 (1993).

[25]P. A. Durbin, "Near-wall turbulence closure modeling without "damping functions"," Theor. Comput. Fluid Dyn., **3**, 1 (1991).

[26]R. Rubinstine and J. M. Barton, "Renormalization group analysis of anisotropic diffusion in turbulent shear flows," Phys. Fluids A, **3**, 415 (1991).

[27]J. C. R. Hunt and A. H. Weber, "A Lagrangian statistical analysis of diffusion from a ground-level source in a turbulent boundary layer," Quart. J. R. Met. Soc., **105**, 423 (1979).

[28]R.A. Handler, E. W. Hendricks, and R. I. Leighton, "Low Reynolds number calculation of turbulent channel flow: a general discussion," Memorandum Report 6410, Naval Research Laboratory, (1989).

[29]A. L. Rovelstad, R. A. Handler and P. S. Bernard, "The effect of interpolation errors on the Lagrangian analysis of simulated turbulent channel flow," to appear in *J. Comput. Phys.*, 1993.

[30]G. T. Csanady, *Turbulent Diffusion in the Environment*, (Reidel, Dordrecht, 1973).

[31]O. Zeman and J. L. Lumley, "Modeling buoyancy-driven mixed layers," J. Atmos. Sci., **33**, 1974 (1976).

[32]J. O. Hinze, *Turbulence*, (McGraw Hill, New York, 1976).

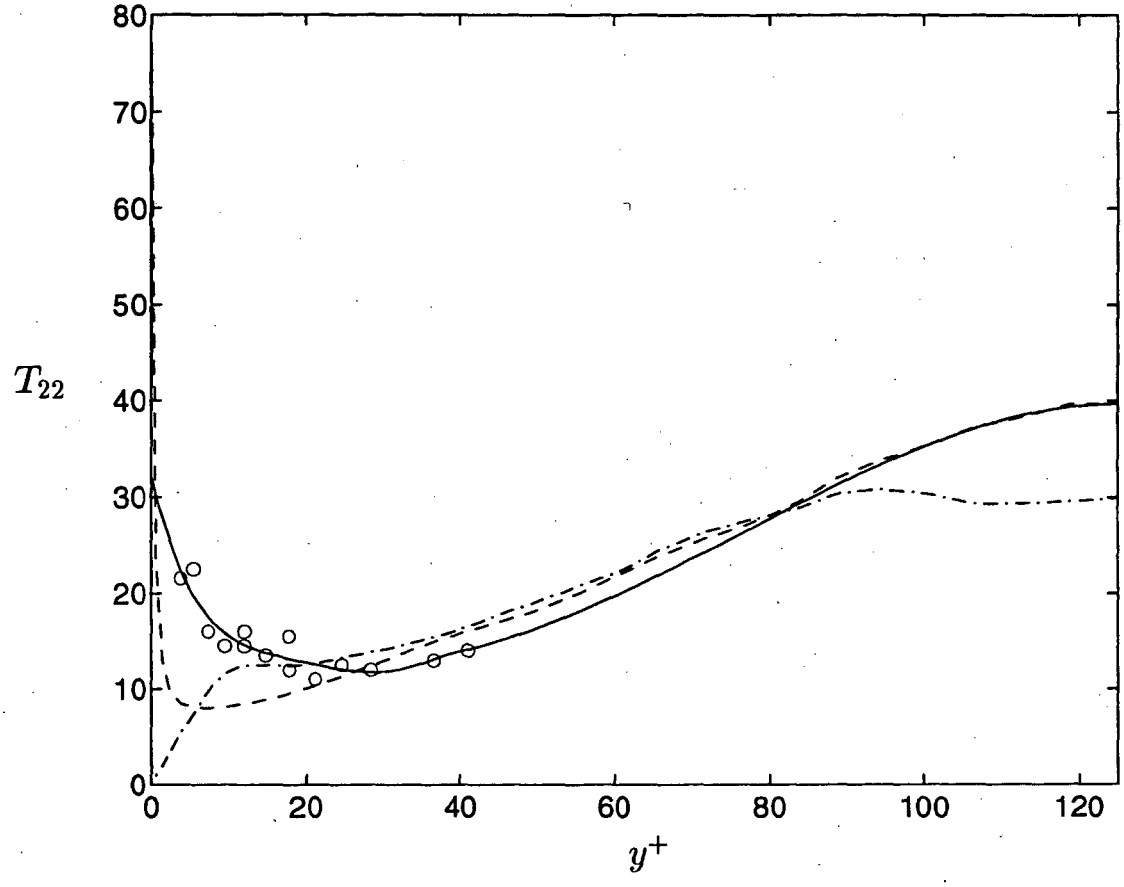

FIG. 1. Lagrangian integral scale T_{22} in channel flow. o, from DNS; —— : fit to DNS; – – – : 'ideal' values; — · — : computed from (19).

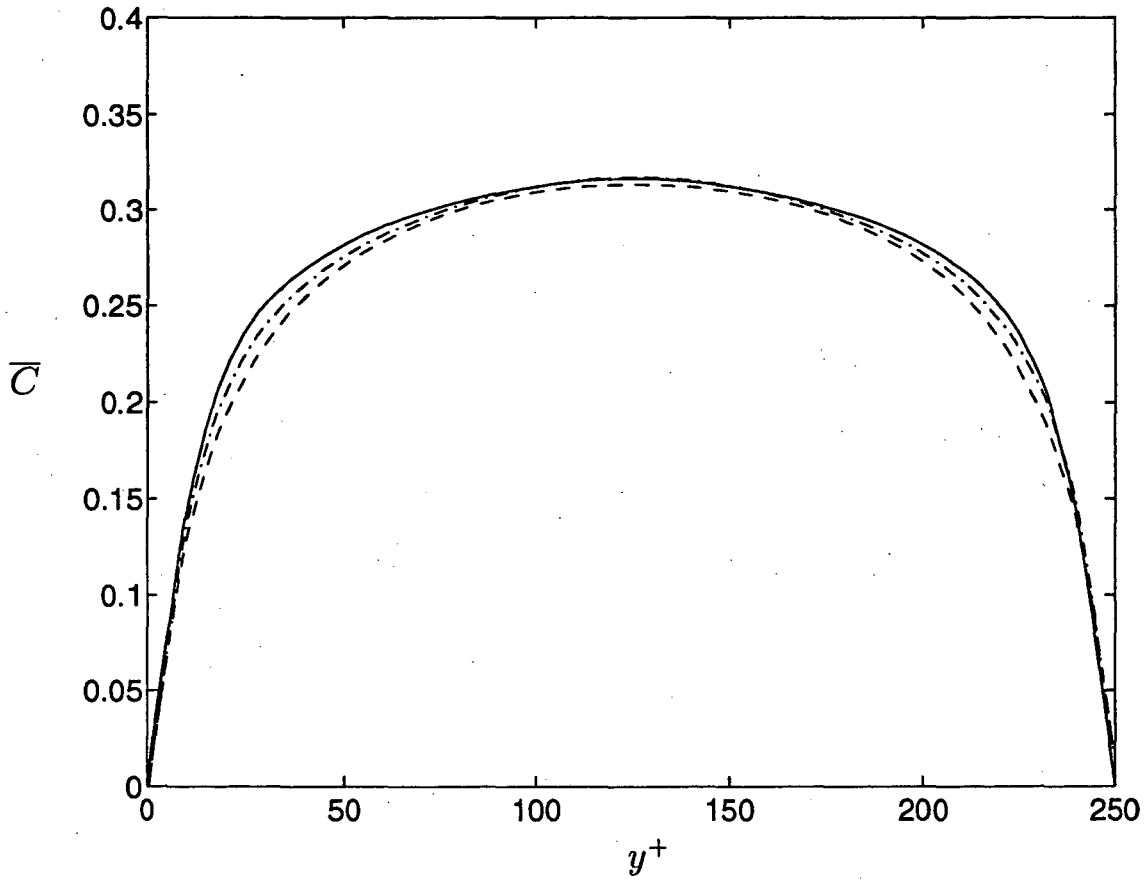

FIG. 2. $\overline{C}$ for uniform source from closure schemes. —— : DNS; - - - : from (17); — · — : from (18).

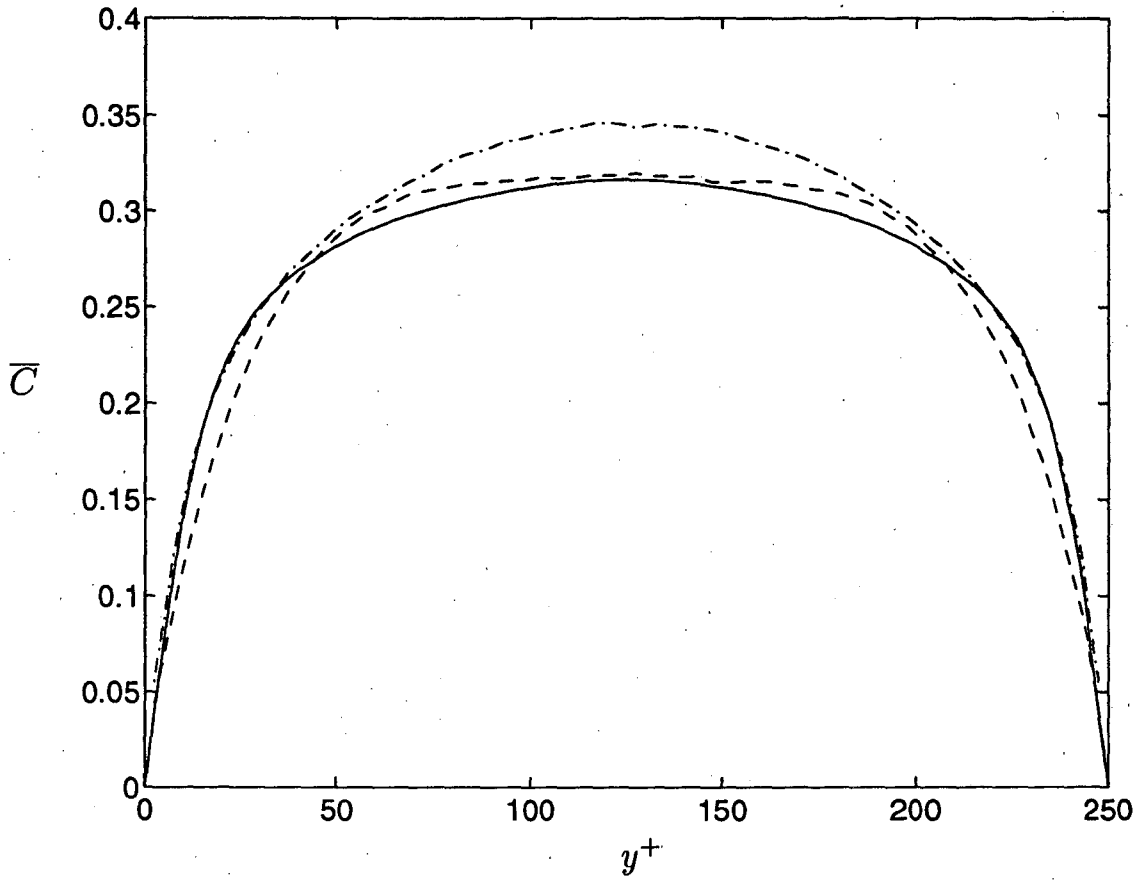

FIG. 3. $\overline{C}$ for uniform source from random flight models. —— : DNS; – – – : from (20), (21); — · — : from (20), (22).

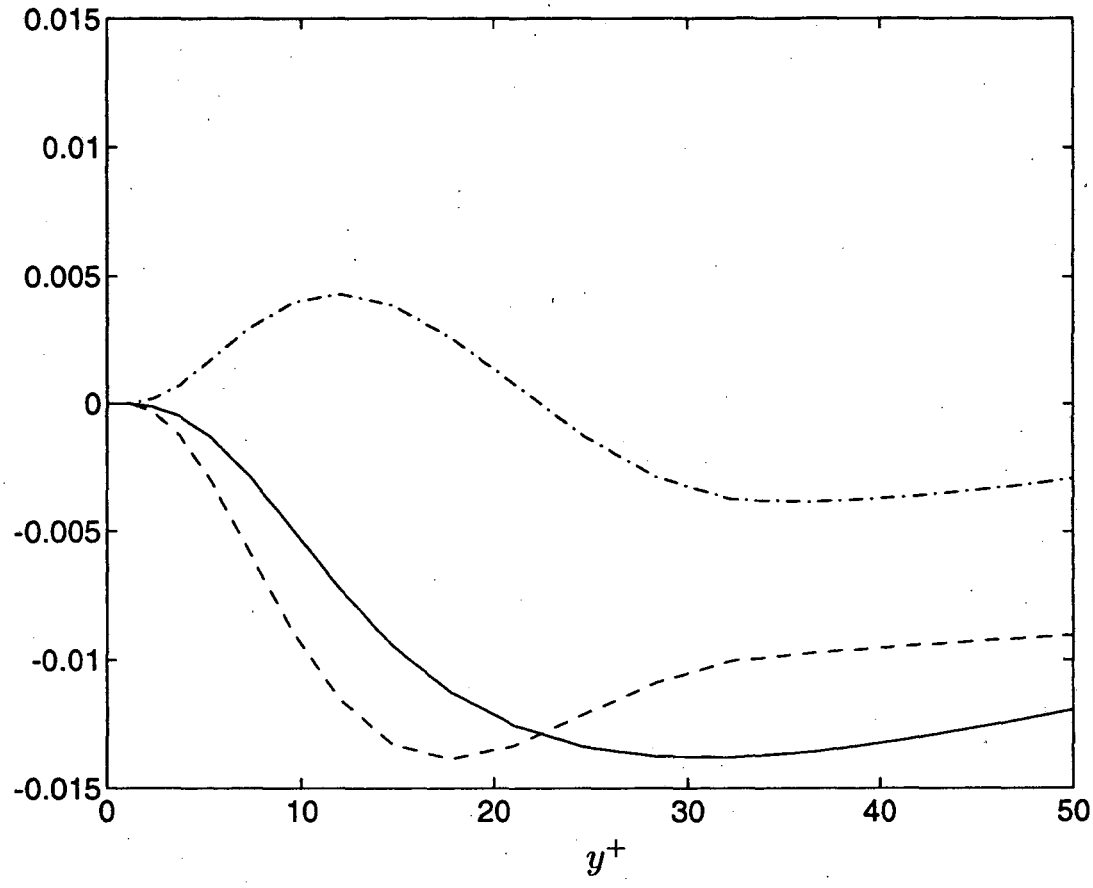

FIG. 4. Lagrangian decomposition of $\overline{vc}$ in uniform source flow. —— : $\overline{vc}$; - - - : gradient contribution from (17); — · — : non-gradient contribution.

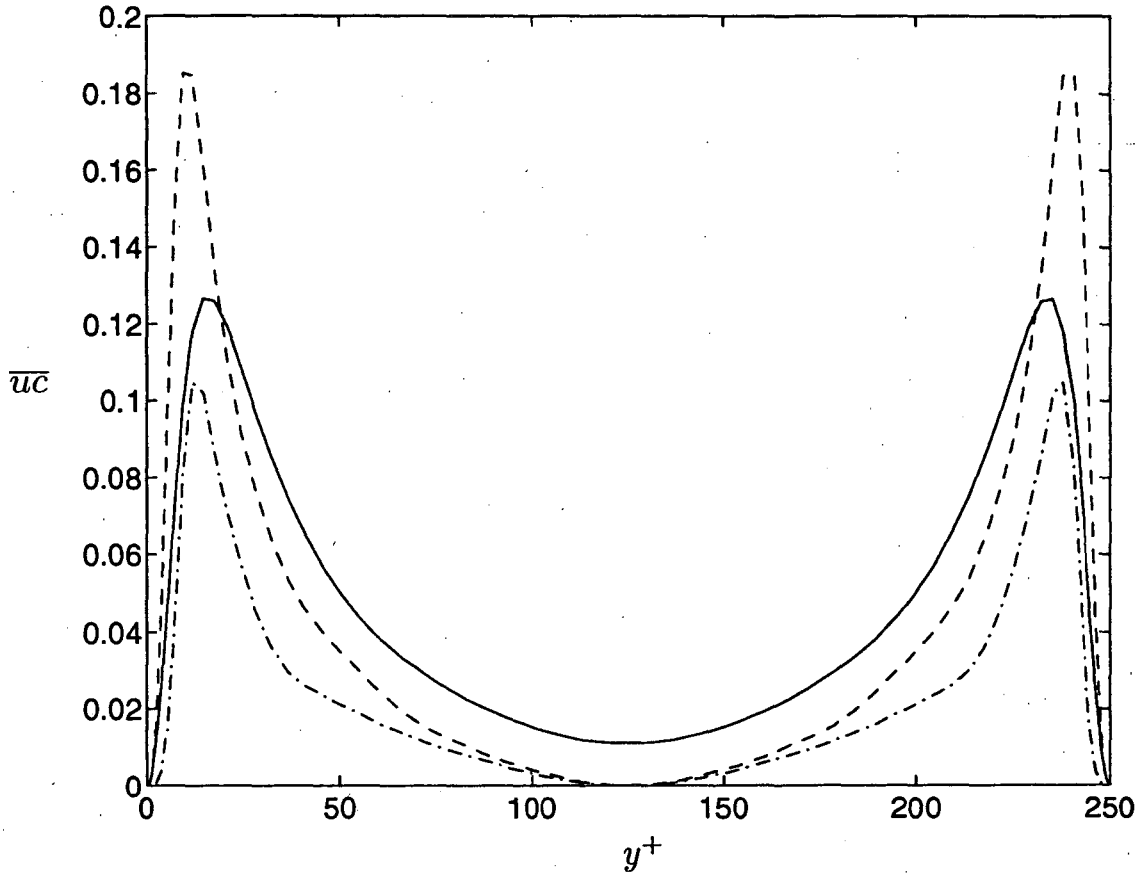

FIG. 5. Comparison of $\overline{uc}$ predictions in uniform source flow. —— : DNS; - - - : from (23); — · — : from (24).

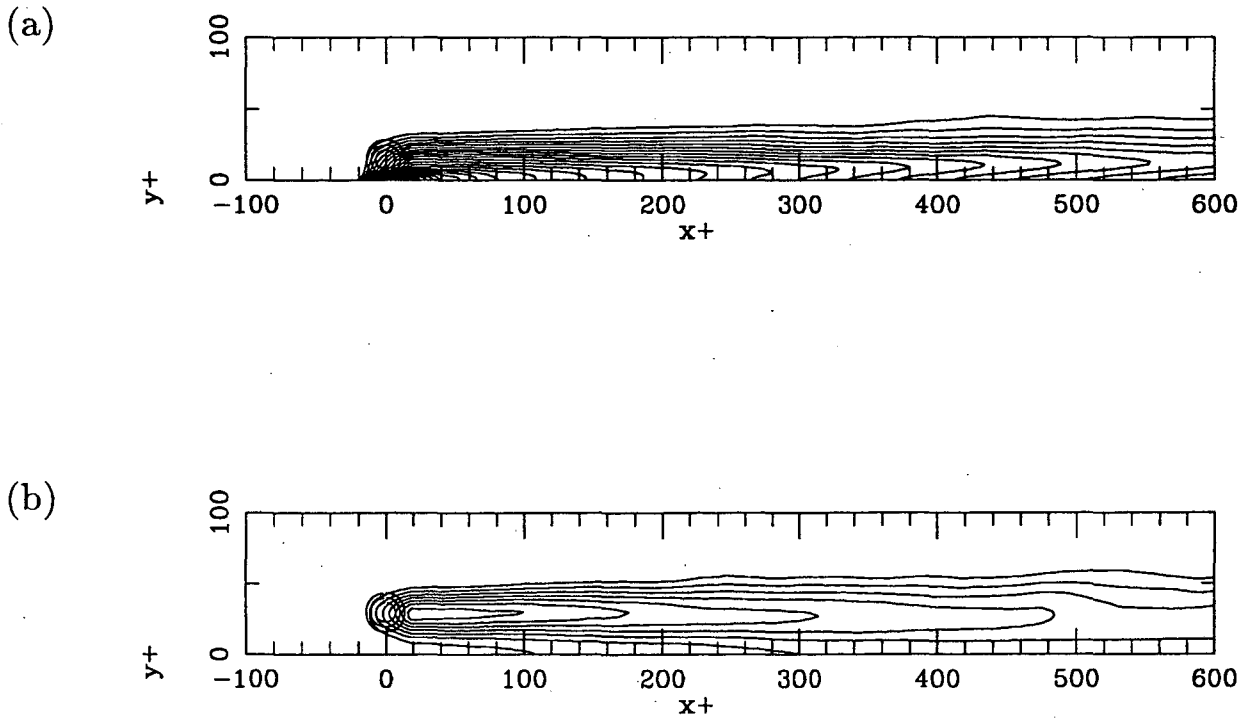

FIG. 6. $\overline{C}$ contours for simulated plume flow. (a) source at $y^+ = 15$, (b) source at $y^+ = 30$.

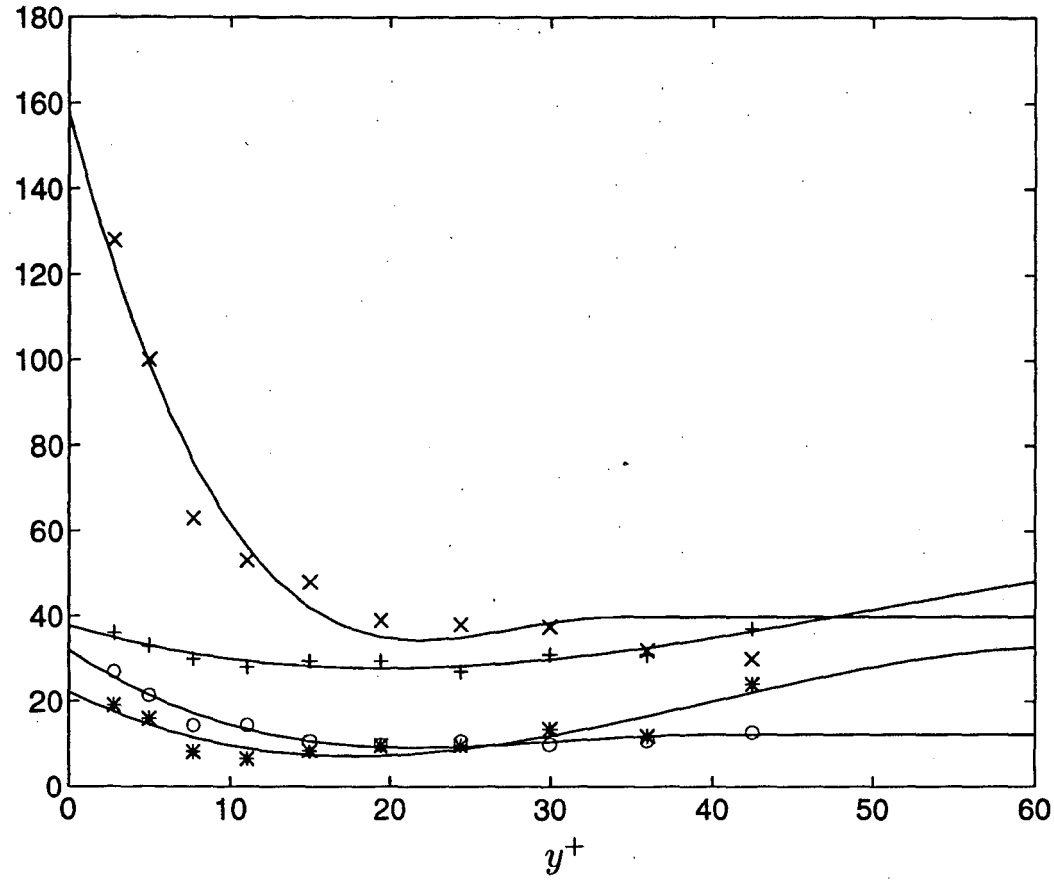

FIG. 7. Lagrangian integral time scales for $R_\tau = 145$ simulation. $+$: T_{11}; $\times$: T_{12}; $*$: T_{21}; $\circ$: T_{22}.

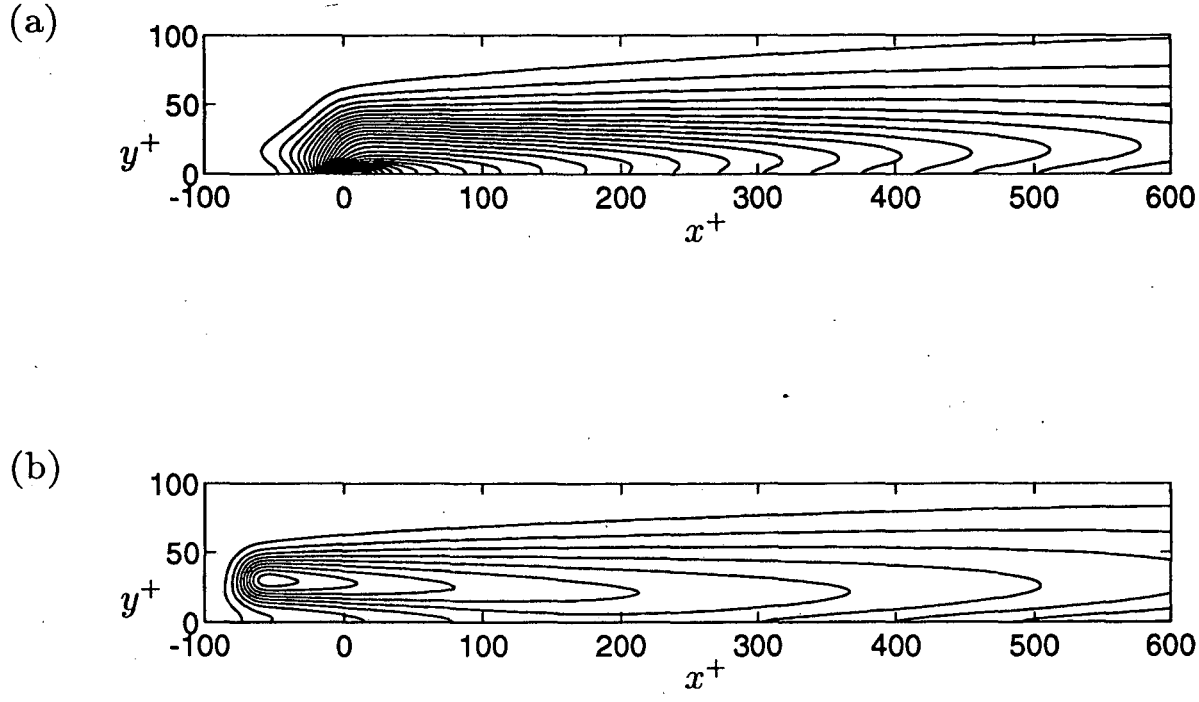

FIG. 8. $\overline{C}$ contours computed using (26) and (27). (a) source at $y^+ = 15$, (b) source at $y^+ = 30$.

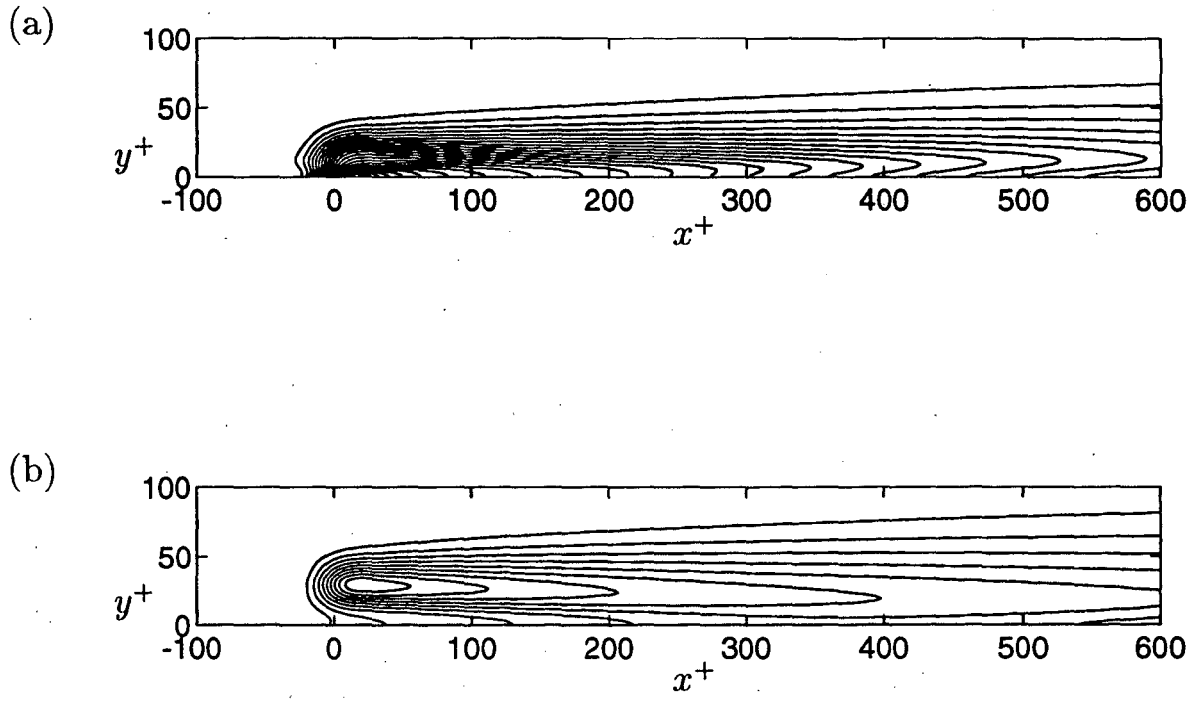

FIG. 9. $\overline{C}$ contours computed using (28) and (29). (a) source at $y^+ = 15$, (b) source at $y^+ = 30$.

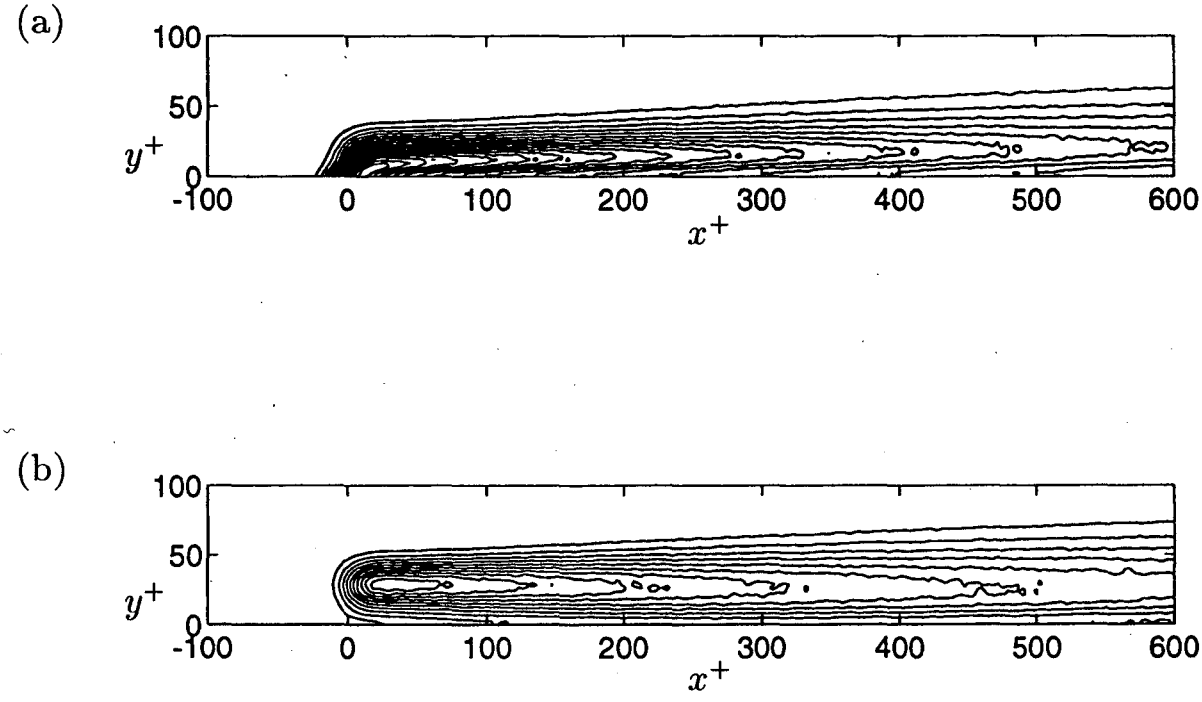

FIG. 10. $\overline{C}$ contours computed using random flight model (30) – (38). (a) source at $y^+ = 15$, (b) source at $y^+ = 30$.

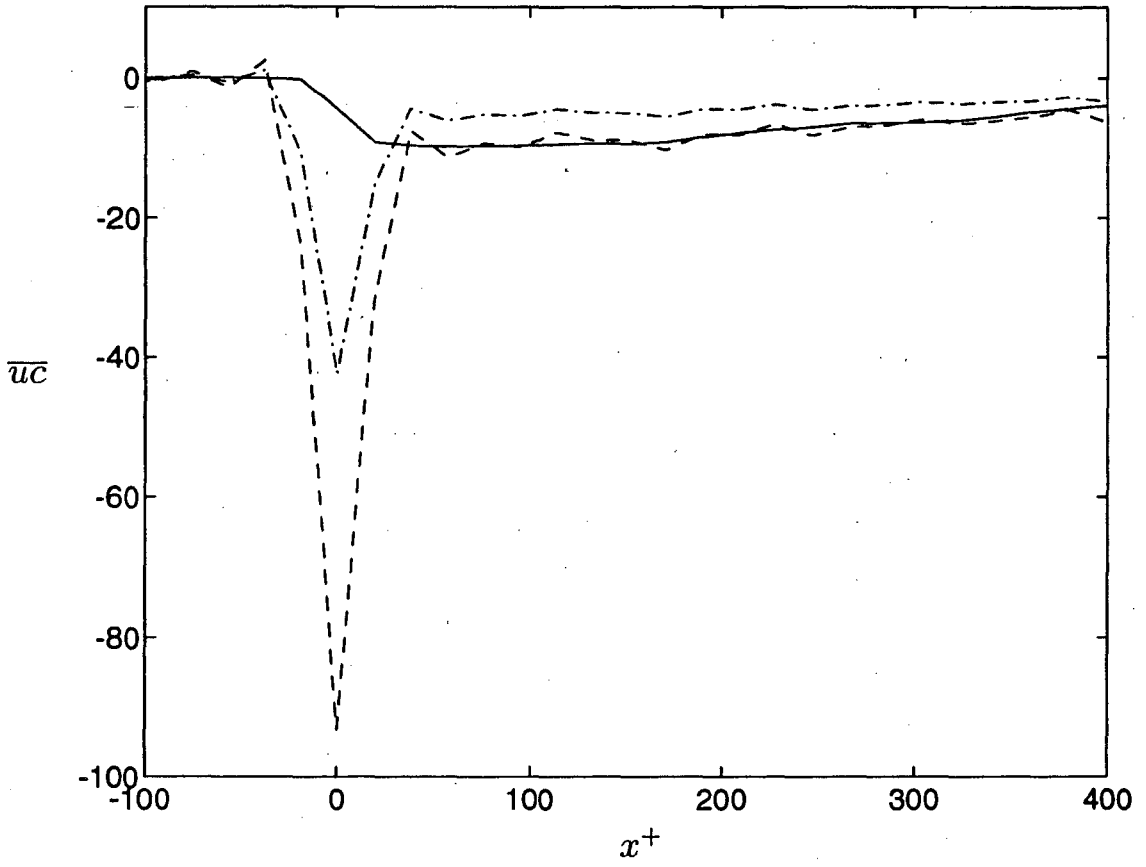

FIG. 11. $\overline{uc}$ for $y^+ = 15$ plume on the line $y^+ = 15$. —— : DNS; - - - : (26) using correct $\overline{C}$; — · — : (28) using correct $\overline{C}$.

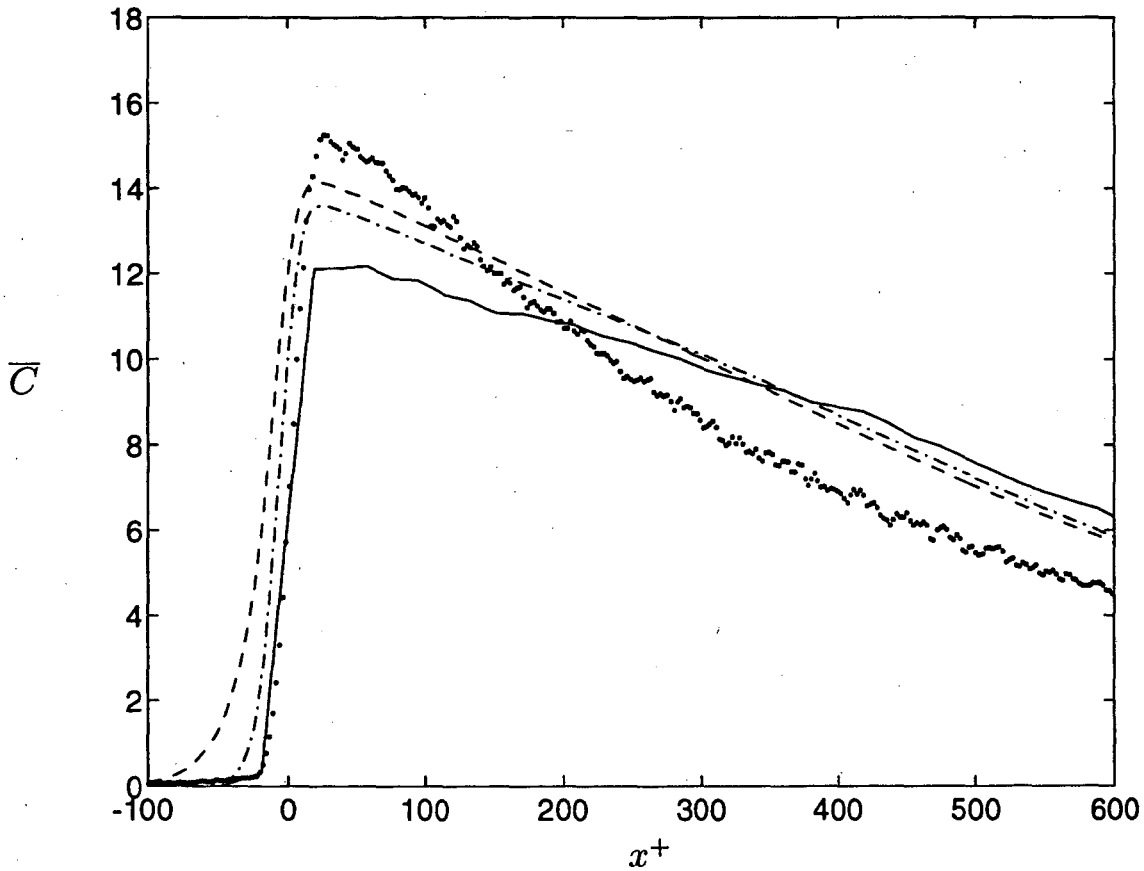

FIG. 12. Comparison of $\overline{C}$ on line $y^+ = 15$ for $y^+ = 15$ plume. —— : DNS; - - - : from (26) and (27); — · — : from (28) and (29); · · · : random flight model.

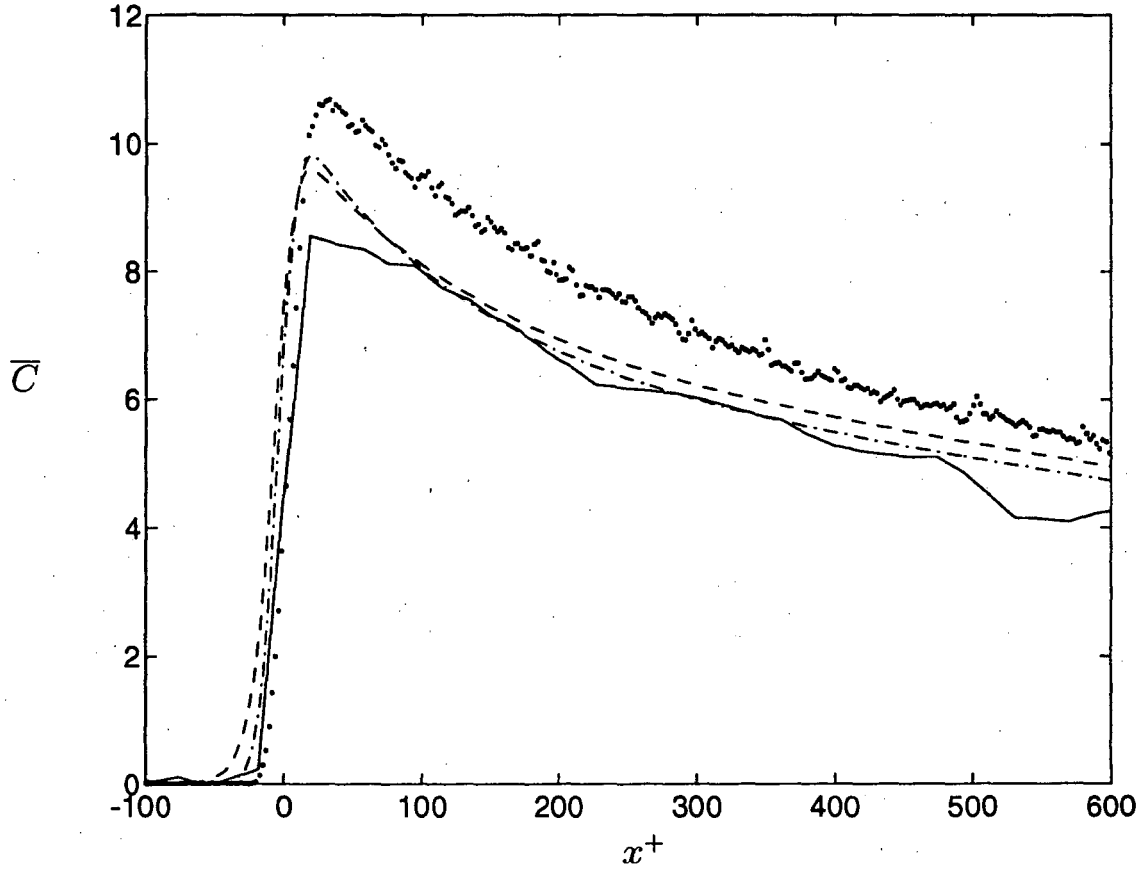

FIG. 13. Comparison of $\overline{C}$ on line $y^+ = 30$ for $y^+ = 30$ plume. —— : DNS; - - - : from (26) and (27) ; — · — : from (28) and (29); · · · : random flight model.

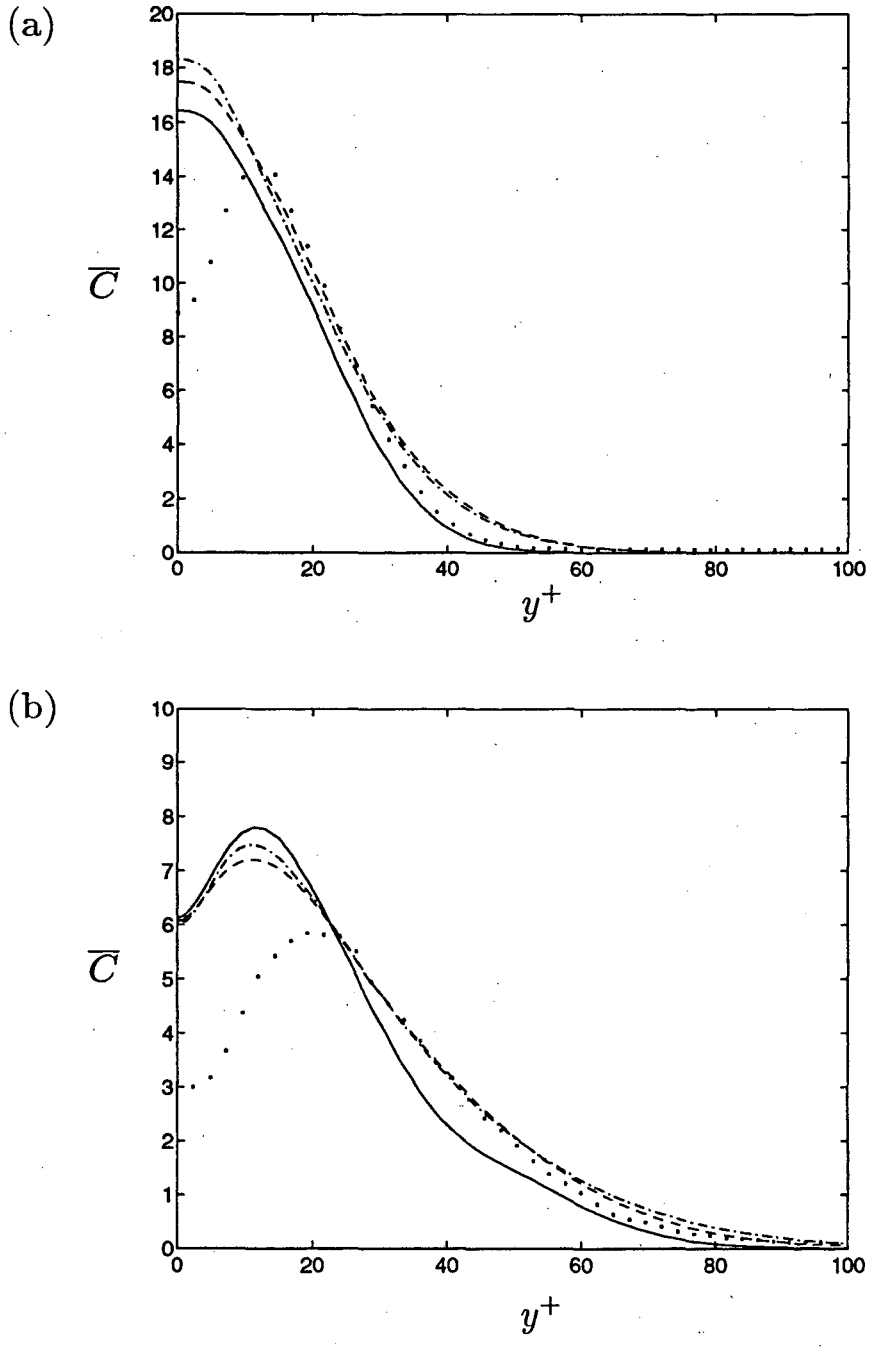

FIG. 14. Comparison of $\overline{C}$ for $y^+ = 15$ plume. —— : DNS; – – – : from (26) and (27); — · — : from (28) and (29); · · · : random flight model. (a) $x^+ = 100$, (b) $x^+ = 500$.

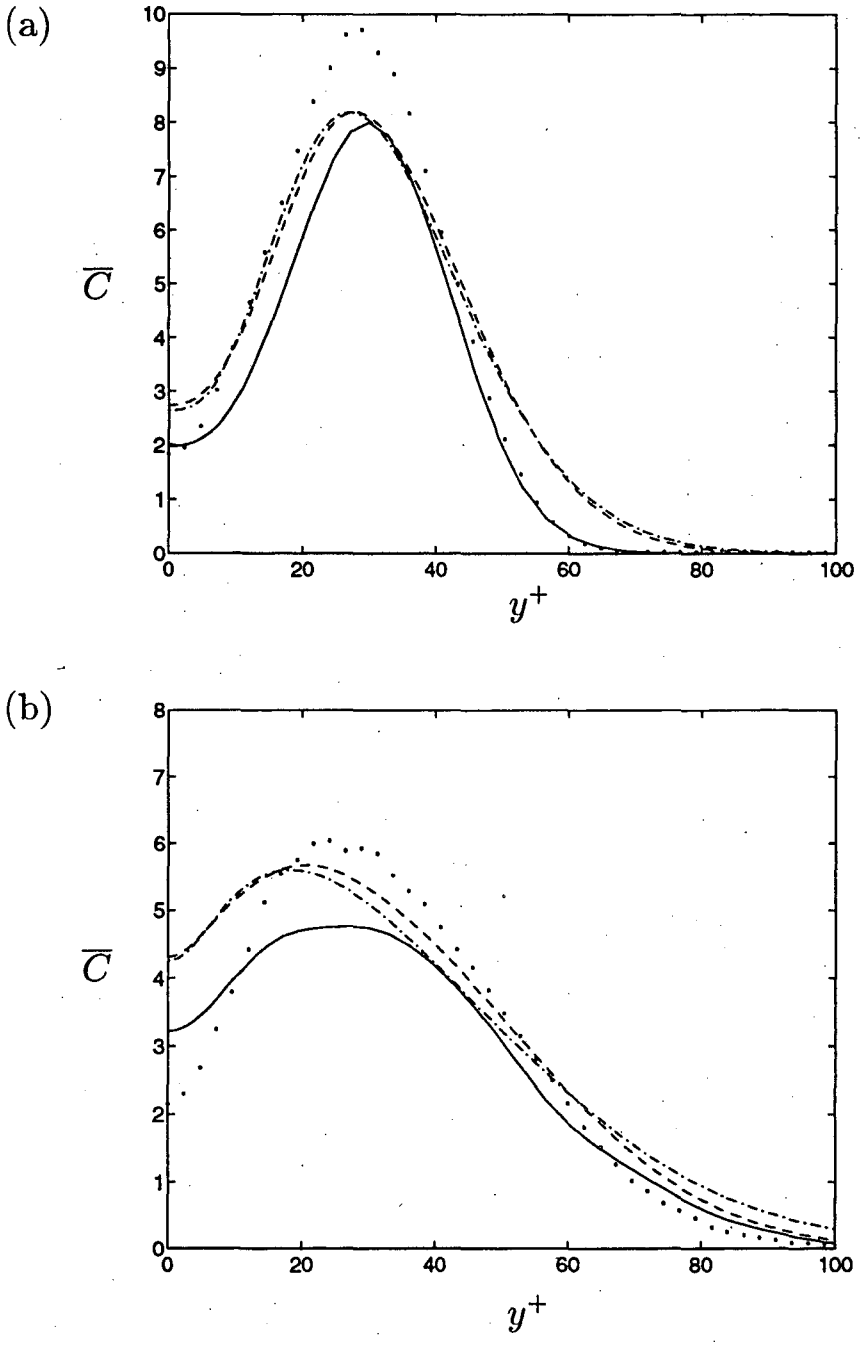

FIG. 15. Comparison of $\overline{C}$ for $y^+ = 30$ plume. —— : DNS; - - - : from (26) and (27); — · — : from (28) and (29); · · · : random flight model. (a) $x^+ = 100$, (b) $x^+ = 500$.

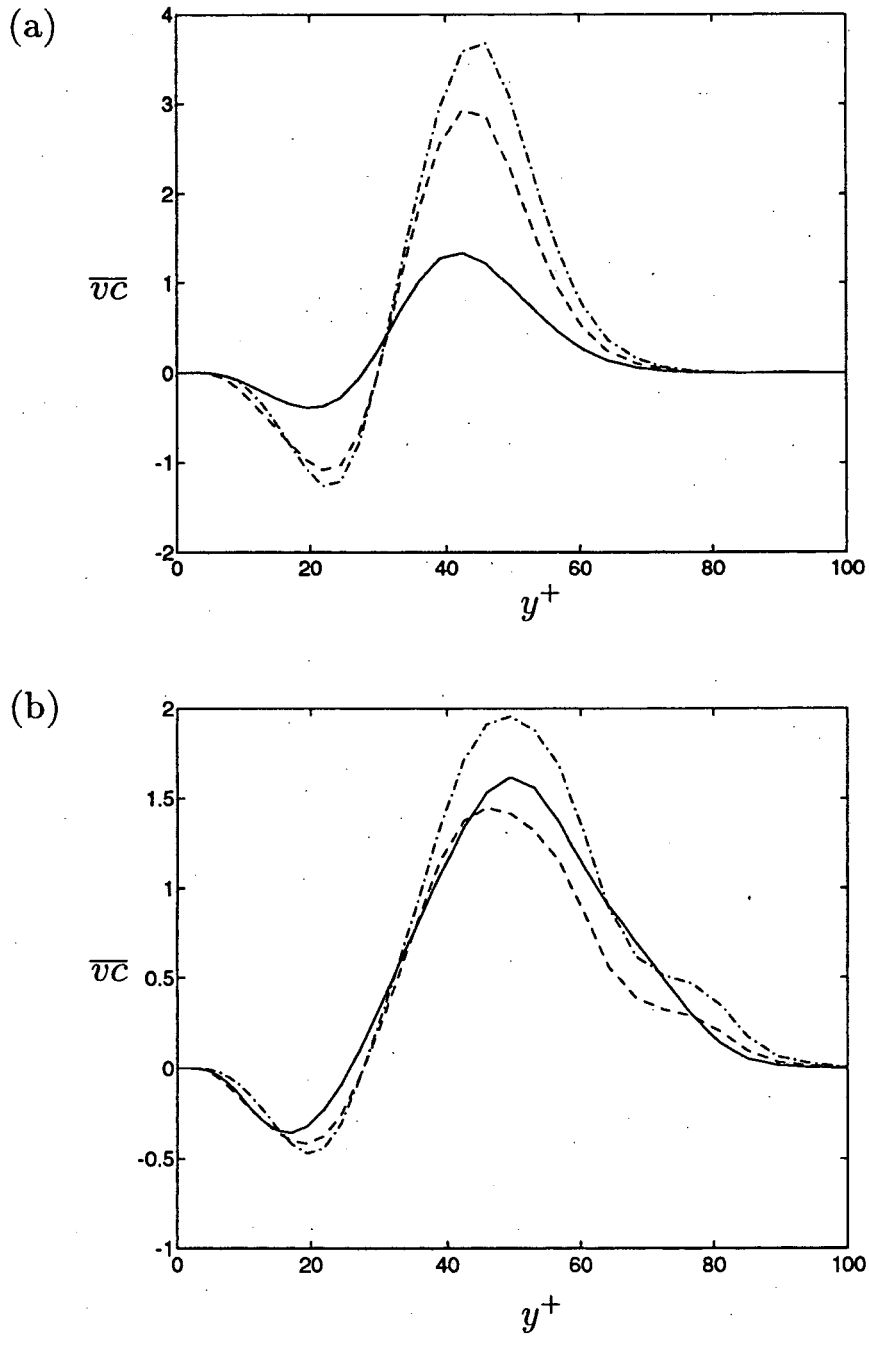

FIG. 16. $\overline{vc}$ for $y^+ = 30$ plume. —— : DNS; - - - : (27) using correct $\overline{C}$; — · — : (29) using correct $\overline{C}$. (a) $x^+ = 100$, (b) $x^+ = 300$.

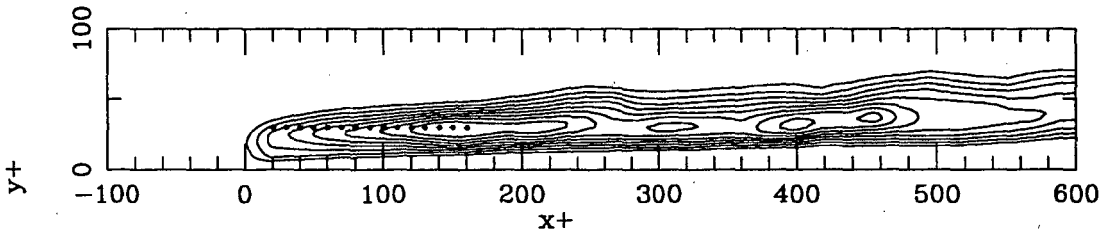

FIG. 17. Contours of $\overline{vc}$ for $y^+ = 15$ plume. Points represent locations where (4) and (41) were evaluated.

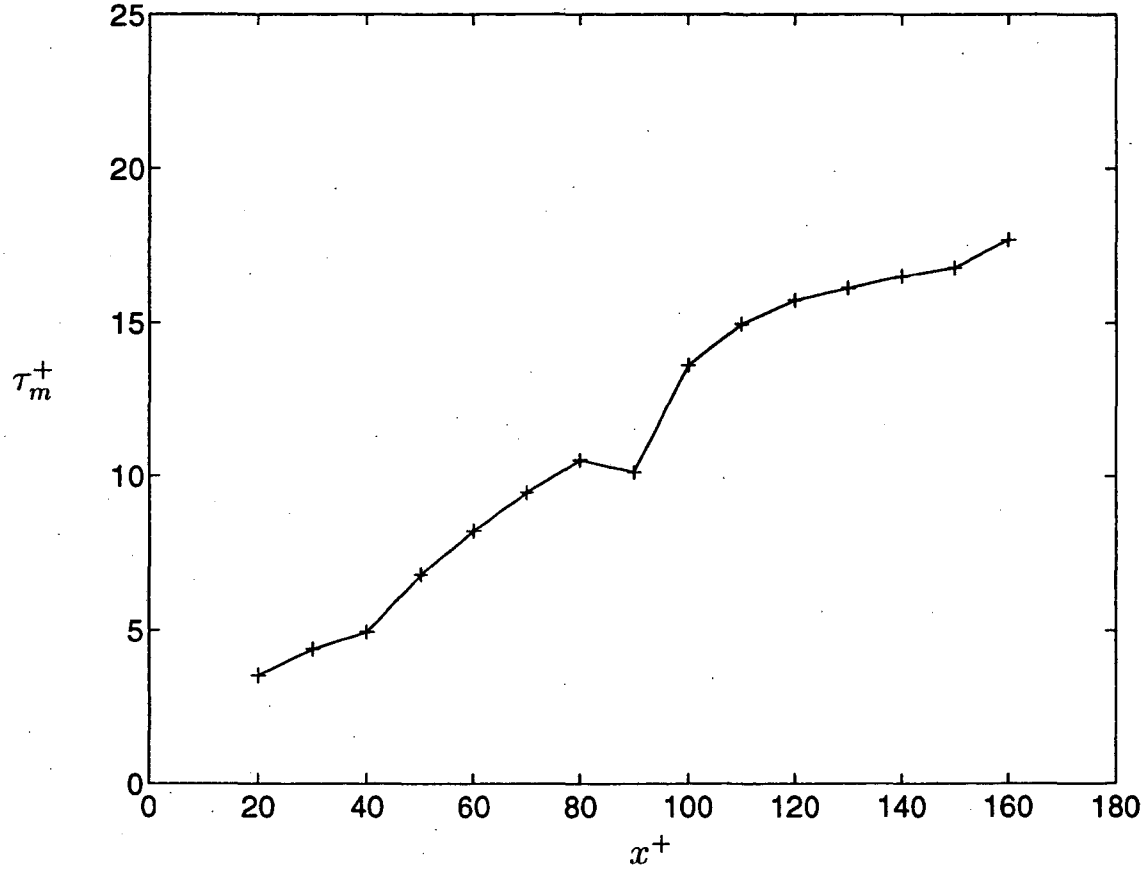

FIG. 18. Mixing time at points in FIG. 17.

(a)

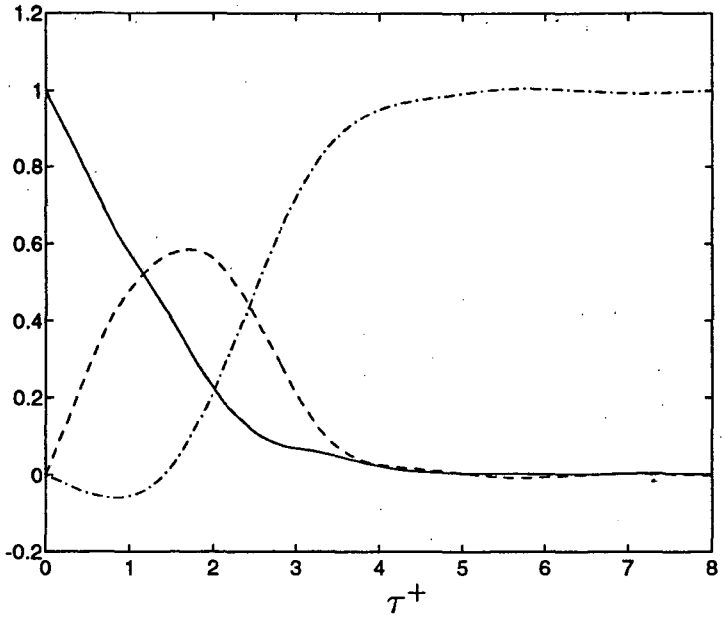

(b)

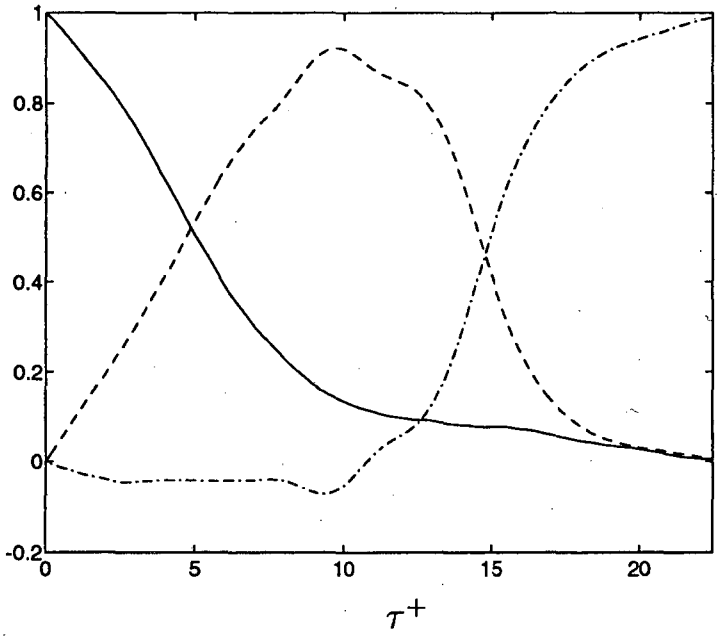

Fig. 19. Evaluation of (4) normalized by $\overline{v_a c_a}$ for $y^+ = 15$ plume. —— : $\overline{v_a c_b}$; - - - : $\overline{v_a(\overline{C}_b - \overline{C}_a)}$; — · — : $\overline{v_a(C_a - \overline{C}_b)}$. (a) $x^+ = 20$, $y^+ = 30$ (b) $x^+ = 160$, $y^+ = 30$.

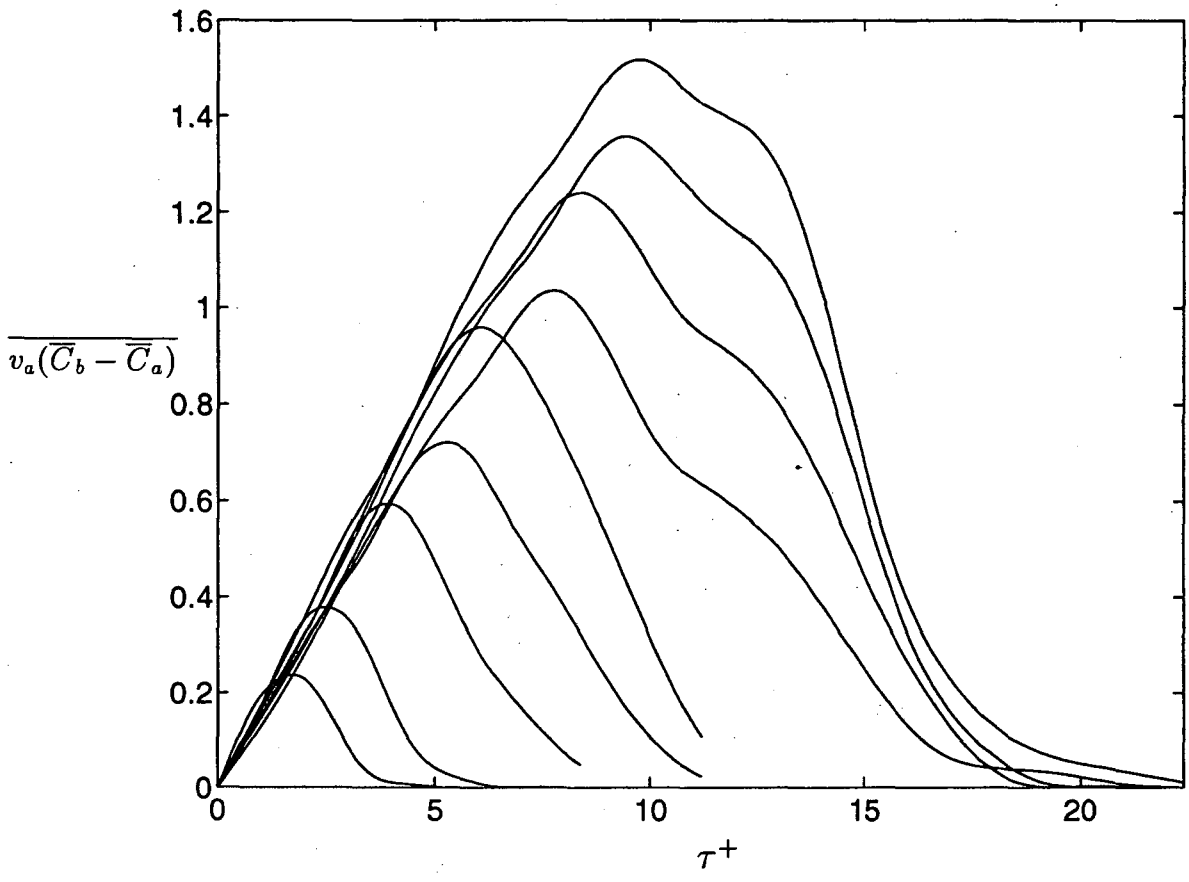

FIG. 20. Displacement transport terms for points in FIG. 17. The curves from smallest to largest peak are for $x^+ = 20, 40, 60, 80, 90, 130, 140, 150, 160$, respectively.

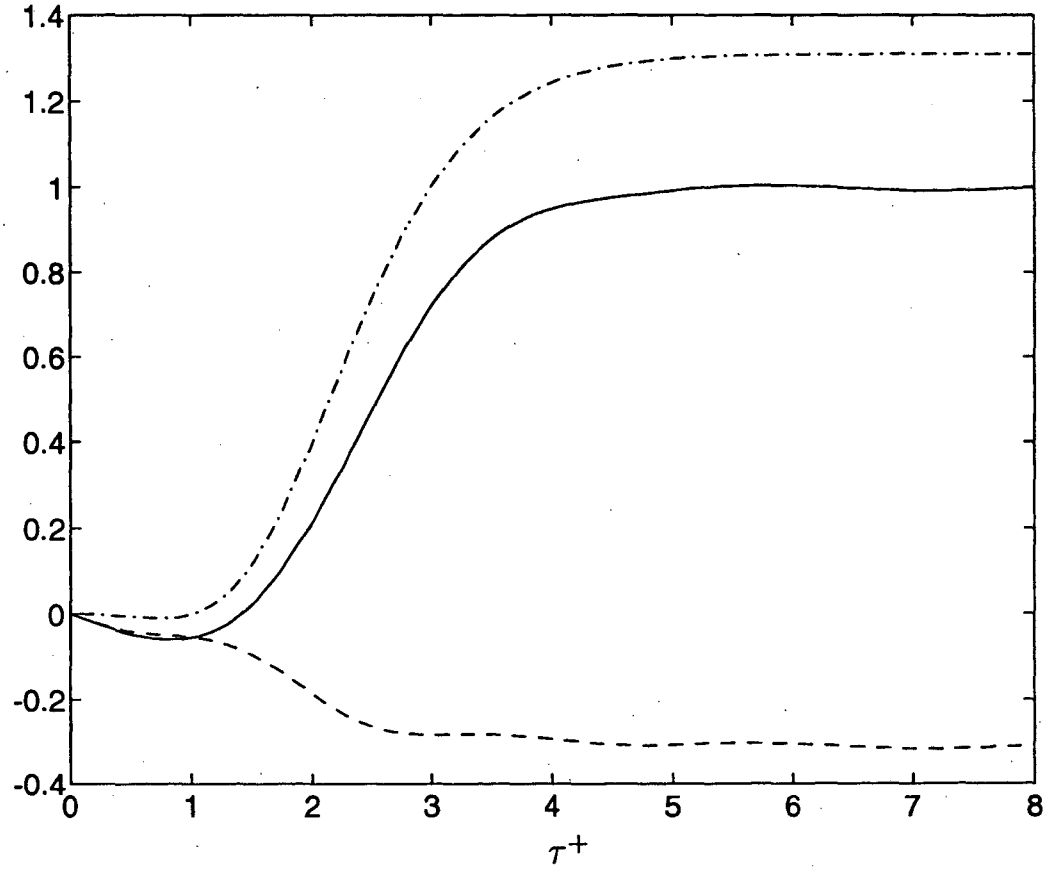

FIG. 21. Evaluation of (41) normalized by $\overline{vc}$ for point $x^+ = 20, y^+ = 30$ in $y^+ = 15$ plume. —— : $\overline{vc}$; - - - : molecular diffusion term; — · — : source term.

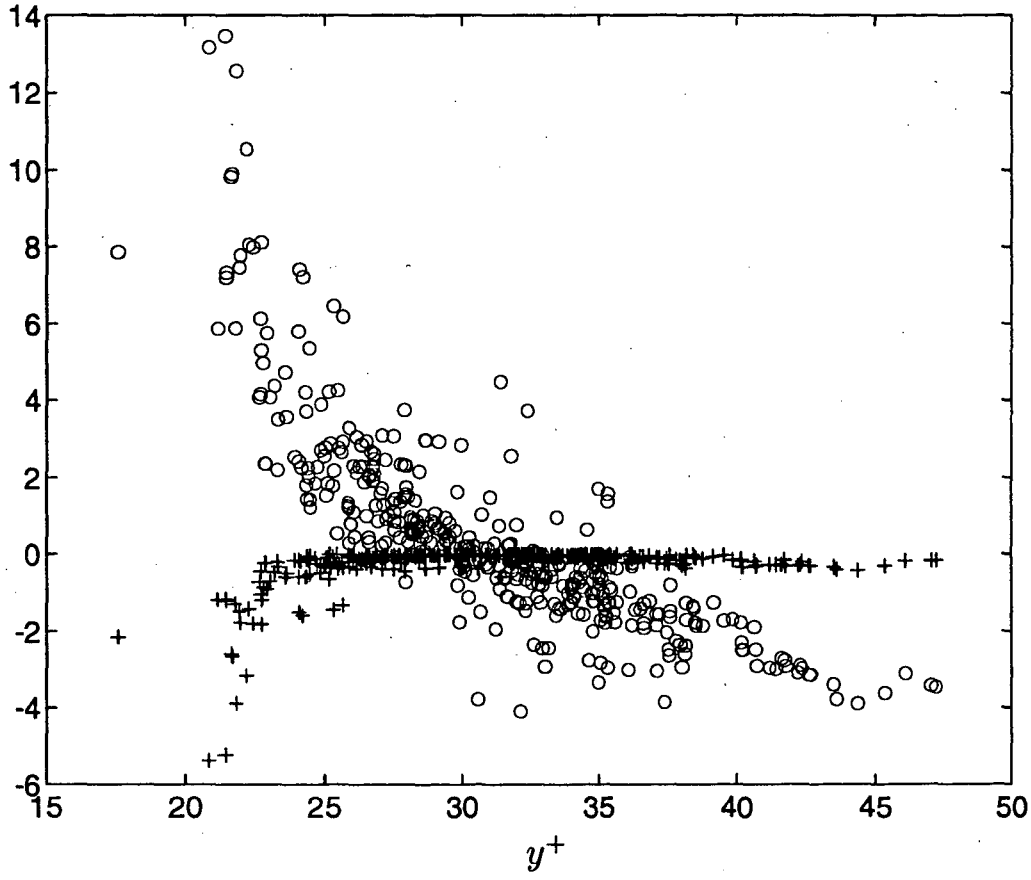

FIG. 22. Individual contributions to $\overline{v_a(C_a - C_b)}$ from paths in ensemble. $\frac{1}{ReSc}\int_{-\tau}^{0} v_a \nabla^2 C(s)ds$: +; $\int_{-\tau}^{0} v_a Q(s)ds$: o.

LAWRENCE BERKELEY LABORATORY
UNIVERSITY OF CALIFORNIA
TECHNICAL INFORMATION DEPARTMENT
BERKELEY, CALIFORNIA 94720